Development of Key Technologies for White Lighting Based on Light-Emitting Diodes (LEDs)

Final Report

Reporting Period Start Date: 1 Oct 2001
Reporting Period End Date: 31 Mar 2004

Principal Authors:

(Lumileds Lighting) Werner Goetz, Bill Imler, James Kim, Junko Kobayashi, Andrew Kim, Mike Krames, Rick Mann, Gerd Mueller, Regina Mueller-Mach, Anneli Munkholm, Jonathan Wierer

(Sandia National Laboratories) Billie Abrams, Andrew Allerman, Bob Biefeld, Katherine Bogart, Randy Creighton, John Emerson, Dave Follstaedt, Dan Koleske, Christine Mitchell, Nancy Missert, Paula Provencio, Lauren Rohwer, Steven Thoma, George Wang, Jess Wilcoxon

Date Issued: June 2004

DOE Award Number: DE-FC26-01NT41251

Lumileds Lighting U.S., LLC
370 West Trimble Rd
San Jose, CA 95131

DISCLAIMER

ABSTRACT

This program was organized to focus on materials development issues critical to the acceleration of solid-state lighting, and was split into three major thrust areas: (1) study of dislocation density reduction for GaN grown on sapphire using "cantilever epitaxy", and the impact of dislocation density on the performance of state-of-the-art high-power LEDs; (2) the evaluation of *in situ* techniques for monitoring gas phase chemistry and the properties of GaN-based layers during metal-organic vapor phase epitaxy (MOCVD), and (3) feasibility for using semiconductor nanoparticles ("quantum dots") for the down-conversion of blue or ultraviolet light to generate white light. The program included a partnership between Lumileds Lighting (epitaxy and device fabrication for high power LEDs) and Sandia National Laboratories (cantilever epitaxy, gas phase chemistry, and quantum dot synthesis). Key findings included: (1) cantilever epitaxy can provide dislocation density reduction comparable to that of more complicated approaches, but all in one epitaxial growth step; however, further improvements are required to realize significant gains in LED performance at high drive currents, (2) *in situ* tools can provide detailed knowledge about gas phase chemistry, and can be used to monitor and control epitaxial layer composition and temperature to provide improved yields (e.g., a fivefold increase in color targeting is demonstrated for 540nm LEDs), and (3) quantum efficiency for quantum dots is improved and maintained up to 70% in epoxy thin films, but further work is necessary to increase densification (absorption) and robustness before practical application to LEDs.

TABLE OF CONTENTS

EXECUTIVE SUMMARY

This is the Final Report of technical work under DE-FC26-01NT41251. The experimental results and discussion are broken up into three sections consistent with the three thrusts of the program: 1) defect studies in III-N materials, 2) in situ tools for improved epitaxial growth of III-nitride materials, and 3) semiconductor nano-particles ("quantum dots") as luminescence centers for down-conversion of blue or UV light into white light.

Reduced dislocation density in GaN has been achieved using a cantilever epitaxy (CE) process developed at Sandia National Laboratories (SNL). Extensive materials characterization both at SNL and at Lumileds Lighting (LL) shows that solid, steady progress has been made in both the quality and uniformity of these epitaxial films as the process evolved from 1st (AlN-based nucleation) to 2nd (GaN-based nucleation) generation. Overall dislocation densities were reduced to below the detection limit of cross-sectional transmission electron microscopy (~1E8 cm^{-2}). Plan view TEM indicates an overall dislocation density < 3e7 cm^{-2} in the best films (with down to < 1e6 cm^{-2} in the 'wing' regions). These numbers were verified using cathodoluminescence and atomic force microscopy techniques for counting dislocations. This compares very favorably against standard industry practice (~1E9-1E10 cm^{-2}). Also, considerable improvement in CE layer uniformity across the wafer was made throughout the year, problematic dislocations loops known as "dark block defects" were identified and eliminated during the second year. LED devices were grown at Lumileds on top of CE and standard starting layers simultaneously, and fully characterized. We found that the CE-based starting layers provided much better external quantum efficiency at low currents, and slightly improved temperature dependence overall. However, at high (operating) currents, the performance of CE-based and standard LEDs was comparable. An investigation into optical performance of the CE starting layers found that residual GaN-based material deposited in the trenches during overgrowth included optically absorbing centers. We postulate that elimination of this material in an improved CE process would increase external quantum efficiency and provide light output gains over and above standard LEDs at high drive currents. Also, at high drive currents forward bias instability and resulting forward current leakage are observed for CE-based LEDs. More effort is needed to identify the source of the leakage and devise solutions to eliminate this problem.)

Several tools were investigated for measuring growth rate, temperature, strain, and composition of (Al,In)GaN films during MOCVD (i.e., in situ). Broadband optical reflectance (BBOR), Multi-beam Optical Stress Sensor (MOSS), and emissivity correcting pyrometry (ECP) tools were installed on a Lumileds research reactor. This situation allowed us to systematically evaluate each tool for in situ determination of film composition. We found that MOSS alone could give an excellent prediction of AlN composition in AlGaN films (within 2%) in a method that should be relatively temperature independent, while BBOR was limited in usefulness because of the small differences in optical constants for small composition changes. For accurate measurements of growth temperature an ultraviolet (UV, ~ 405 nm) pyrometry system was developed at Sandia and transferred to a research reactor at Lumileds, for use in combination with a new topside infrared pyrometer developed at Lumileds. These two tools were used in combination to determine growth temperature in situ, and exploited to demonstrate improved color control for green LEDs, a significant challenge in manufacturing. The use of these two tools, compared to running "blind", resulted in a fivefold improvement in color control targeting for 540 nm, a major achievement. These pyrometers are now being investigated for use in a production multi-wafer reactor at Lumileds. At Sandia, a model for the MOCVD growth mechanisms of AlGaN was developed, using a relatively simple mechanism employing the CHEMKIN/NIKE approach. About half of the mechanism involves particle nucleation chemistry, and half involves particle growth. This current model predicts AlN within ± 2% for the majority of data. Finally, also at Sandia, Fourier transform infra-red (FTIR) spectroscopy and quantum chemistry calculations were employed to study the interaction of the Mg precursor with NH_3. This work showed the formation of ammonia-magnesocene adducts which are identified as Lewis acid-base complexes, which may be responsible for anomalous Mg dopant incorporation issues in GaN MOCVD such as the well known "Mg memory effect".

Semiconductor nano-particle "quantum dots" (QDs) were synthesized at Sandia and incorporated into thin films, which were then evaluated for potential application to high power LEDs. The synthesis process involved metathesis reactions starting with simple salt precursors, with the QDs grown at room

temperature. Room temperature synthesis enables slow growth of monodisperse QDs with potentially fewer defects and 90-100% product yield. CdS-based quantum dots showed emission from the blue to red, with best-effort material exhibiting a quantum efficiency of 76% in solution. While incorporation into silicone was not successful to date, incorporation into an epoxy thin film was demonstrated, with quantum efficiency maintained to 70% for one sample. Significant increase in QD density was achieved, with QD thin film absorption length increased from several cm down to below 2 mm. Further densification resulted in lower quantum efficiency, highlighting a key challenge for application of QDs to LEDs. Even so, QDs in epoxy were applied to high power LEDs at Lumileds for the first time. While the absorption was not high enough to dominate the emission spectra, we were able to characterize the temperature dependence and degradation of QD luminescence, highlighting future opportunities for the development of this field.

Progress vs. (budget period) BP1 and BP2 goals are summarized in Tables I & II, respectively. The color coding represents success against meeting milestone targets: green = exceeded target, yellow = met or partially met target, red = did not meet target. Strong progress against these aggressive milestones was achieved.

TABLE I. Progress vs milestones for Budget Period 1 (BP1); reprinted from BP1 Final Report.

I. Defect Studies Item	Measure	Industry Practice	YEAR 1 Program Target	12 MONTHS Progress
I-A. Dislocation Density Reduction	Etch-pit or plan-view TEM counting	10^10 cm^-2	wing: < 1 E 6 overall: < 3 E 8	wing: ~ 1 E 6 (edge+mixed) overall: ~3 E 7 to 1 E 8
1-B. Percent device area of low dislocation density (<10^6 cm^-2) material	Etch-pit or plan-view TEM counting	0%	> 50%	70% (wing region)
I.C Cantilever epi (CE) width of post to nucleate growth	Optical microscopy or SEM	n/a	< 2um	~ 1 um
I-D. Electrical properties of GaN layers on CE substrates	300K mobilities via Hall measurements	GaN:Si (1E18) μ~200 cm^2/Vs GaN:Mg (1E19) μ~6 cm^2/Vs	> 300 > 10	nm 8.5
I-E. Efficiency enhancement of III-N LEDs	Relative QE measured for III-N LEDs at 100 A/cm^2 on CE substrates compared to non-CE	1.0x (normalized to non-CE-substrate devices)		

II. In Situ Tools Item	Measure	Industry Practice	YEAR 1 Program Target	12 MONTHS Progress
II-A. Composition monitoring using broadband reflectance	Correlation coefficient: composition by XRD to reflectance parameter(s)	n/a	R^2 > 0.70	R^2 ~ 0.99 (few data pts)
II-B. Strain vs composition monitoring using MOSS	Correlation coefficient: strain by XRD to MOSS parameter(s)	n/a	R^2 > 0.70	AlGaN / GaN: R^2 ~ 0.96 InGaN / GaN: R^2 ~ 0.87
II-C. Run-to-run active region growth temperature control	PL (HeCd) peak wavelength for green (>530 nm) LEDs over 3 runs	range: 40 nm		
II-D. AlGaN deposition chemistry (for Al x: 10 to 20%)	Predictive model based on chemical mechanism for parasitic reactions	n/a		

III. Quantum Dots Item	Measure	Industry Practice	YEAR 1 Program Target	12 MONTHS Progress
III-A. Demonstrate high efficiency QDs in non-aqueous solution	QE with excitation at ~ 400-460 nm	QE: 30-50%	50%	28%
III-B. Demonstrate high absorption in QDs dispersed in thin film	Absorption length of excitation at ~ 400-460 nm	n/a		
III-C. Demonstrate blended QDs for white emission	QD spectrum + blue LED emission color rendering index (CRI)	n/a		
III-D. Encapsulation for QDs	Degradation characteristics under 85C/60%RH.	n/a		
III-E. Prototype White LEDs employing QDs with CRI > 80	Conversion efficiency: White LED power (mW) ratio to standard blue LED (mW)	n/a		
III-F. Optical Properties of QDs in Thin Films	Optical backscatter/luminescence measurements.	n/a	Absorption > 30%. Backscatter < 5% of pump intensity. Pump wavelengths of ~400 and ~460 nm.	Absorption < 1 % Backscatter < 0.1% (dilute thin films) 405 nm pump

TABLE II. Progress vs milestones for Budget Period 2 (BP2).

I. Defect Studies Item	Measure	Industry Practice	**YEAR 2** Program Target	**24 MONTHS** Progress
I-A. Dislocation Density Reduction	Etch-pit or plan-view TEM counting	10^10 cm^-2	**wing: <10^6 cm^-3** **overall: <10^8 cm^-3**	**wing: 0.9 x 10^6 cm^-3** **overall: 3-7 x 10^7 cm^-3**
I-E. Efficiency enhancement of III-N LEDs	Relative QE measured for III-N LEDs at 100 A/cm^2 on CE substrates compared to non-CE	1.0x (normalized to non-CE-substrate devices)	**1.5x**	**> 1.5x (low currents)**

II. In Situ Tools Item	Measure	Industry Practice	**YEAR 2** Program Target	**24 MONTHS** Progress
II-C. Run-to-run active region growth temperature control	PL (HeCd) peak wavelength for green (>530 nm) LEDs over 3 runs	range: 40 nm (actually 50 nm)	**range: 10 nm**	**range: 13.5 nm (over six runs)**
II-D. AlGaN deposition chemistry (for Al x: 10 to 20%)	Predictive model based on chemical mechanism for parasitic reactions	n/a	**Predict AlGaN layer Al composition to within +/- 2% (absolute) as a function of reactor temperature and pressure.**	**18 of 20 runs (Al% < 20%)**

III. Quantum Dots Item	Measure	Industry Practice	**YEAR 2** Program Target	**24 MONTHS** Progress
III-A. Demonstrate high efficiency QDs in non-aqueous solution	QE with excitation at ~ 400-460 nm	QE: 30-50%	**50%**	**76% (and 70% in epoxy film)**
III-B. Demonstrate high absorption in QDs dispersed in thin film	Absorption length of excitation at ~ 400-460 nm	> 10 mm	**100 um**	**1.9 mm**
III-C. Demonstrate blended QDs for white emission	QD spectrum + blue LED emission color rendering index (CRI)	n/a	**CRI > 80**	**inter-absorption effects**
III-D. Encapsulation for QDs	Degradation characteristics under 85C/60%RH.	n/a	**Degradation comparison: at 50A/cm^2, for 168 hours.**	**n/a**
III-E. Prototype White LEDs employing QDs with CRI > 80	Package Loss: 1-CE/(QExQD), where CE = conversion eff., QE = quant. eff., and QD = quant. deficit	50% (phosphors)	**<50%**	**absorption too low at present**
III-F. Optical Properties of QDs in Thin Films	Optical backscatter/luminescence measurements.	n/a	**Absorption > 50%. Backscatter < 2% of pump intensity.**	**Absorption ~ 80%. Backscatter ~ 5%.**

Color Code:

	met/exceeded target
	substantial progress against target
	did not meet target

I. DEFECT STUDIES

I-A. Motivation

The key motivation for this work is to understand the role of dislocations on the performance of high power state-of-the-art InGaN/GaN LEDs. Sapphire is the typical substrate of choice for III-nitride optoelectronic device manufacture, due to its compatibility with the harsh environment of III-nitride metalorganic chemical vapor deposition (MOCVD) as well as its wide availability and relatively low cost. However, GaN is not lattice matched to sapphire and, if no special precautions are taken, threading dislocation densities (TDDs) from the lattice-mismatched heteroepitaxy can be the range of ~ 1E10 cm^{-2}. Currently, growth techniques in industry typically provide TDDs in the range of 1E9 cm^{-2}. While reasonably high-performing devices (i.e., InGaN/GaN LEDs), are obtained in spite of the high density of dislocations, the fact that their mean spacing is less than 1 um, and thus likely comparable to the diffusion length of minority carriers, suggests that they may negatively impact device performance. A systematic comparison, between similar device structures of varying TDD, is an important undertaking and perhaps essential to determine whether III-nitride devices are realizing their full potential. In this program, we compared a novel dislocation density reduction technique developed at Sandia National Labs ("Cantilever Epitaxy"), to standard epitaxial techniques employed at Lumileds, to determine the role of TDD in high power InGaN/GaN LED performance. These investigations involved the characterization of full LED structures, with varying In composition, at elevated current densities and temperatures, in order to obtain a complete picture of the effects of dislocations on high power LEDs under true operating conditions. In order to obtain the best possible comparison, template GaN layers (either Cantilever or standard) were placed side-by-side in a single MOCVD reactor such that the LED device epitaxial layers were simultaneously grown on both templates. Further, we note that the run-to-run performance repeatability of the chosen reactor is good by Lumileds' standards, further increasing our confidence level in the comparisons made.

I-B. Cantilever Epitaxy

Cantilever Epitaxy (CE) was invented at Sandia just before the initiation of this program [1]. This prior work showed that greatly reduced dislocation densities were possible with this method. CE also offered a significant advantage over other methods to reduce dislocation densities: ***CE can be accomplished with a single growth in the MOCVD reactor.*** Sandia has now received a patent on this growth process [2]. However, the detailed growth techniques needed development to obtain reduced defect densities over large areas as needed for devices development. Moreover, the benefits of using CE-GaN for light emission were yet to be demonstrated through growth of LEDs on CE wafers. In the following section the improved CE growth method and several technical achievements in the development of improved, lower defect density layers are described.

Description of Cantilever Epitaxial Growth of GaN

The basic CE growth process consists of the following steps. First, trenches are etched into the substrate leaving stripes of mesas along the [1-100] direction. Etching trenches into the very resistant sapphire (Al_2O_3) is accomplished by using a quad level resist and etching with an inductively-coupled plasma using BCl_3. Vertical growth of the over-layer is then initiated on the mesas; this material is epitaxial with the substrate but contains dislocations. After some vertical growth, the conditions of the reactor are adjusted to produce lateral growth over the trenches; this lateral ("cantilever") material is suspended from the mesas and does not contain vertical threading dislocations (VTDs) because it is not in contact with the substrate. After adjacent cantilevers are grown together, the continuous solid is grown vertically to produce the desired thickness of the layer material. The basic process flow is illustrated in Fig. 1. In the end, VTDs produced by contact with the substrate are confined to mesa areas, but the cantilever regions over trenches

have very low dislocation densities. In the initial version of the method, the trench width and mesa width were comparable, giving total overall reductions of ~1/2. This approach could be adequate if devices are placed only within the dislocation-free cantilever regions, but achieving broader areas with low overall density requires reducing dislocations over mesa and coalescence areas also.

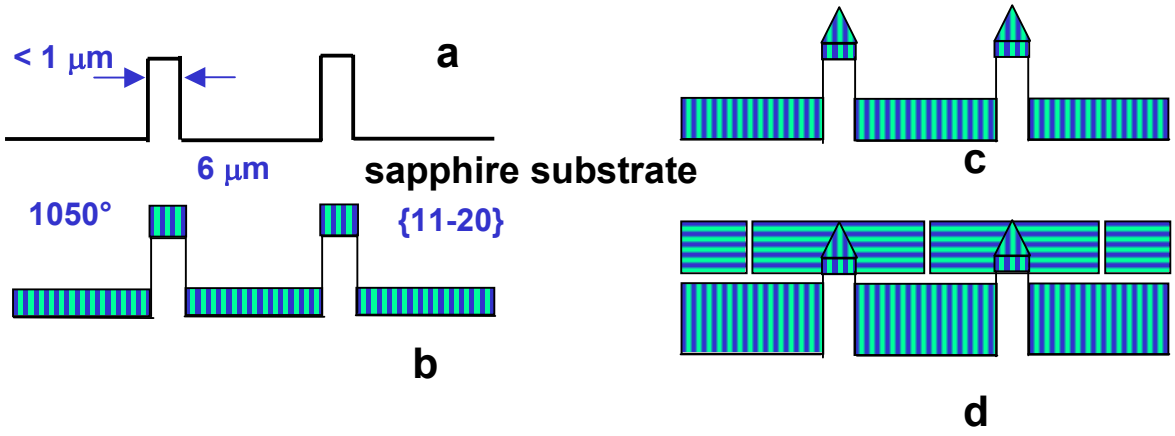

Figure 1. A schematic illustrating the cantilever epitaxy process. The sapphire substrate is etched in (a), the nucleation layer is grown in (b), the initial GaN layer growth is shown in (c) in which the microstructure over the mesas is formed and helps to control the evolution of threading dislocations and, finally, the coalescence is illustrated in (d).

Reducing Dislocation Density by Growth on Narrow Mesas and by Facetted Growth

Early on in the growth of CE layers, VTDs within 0.5 μm of the mesa edge were seen to turn horizontally and not thread to the top of the GaN layer. (See Fig. 2.) These observations led to the concept that a mesa 0.1 μm wide might have fewer dislocations that thread to the top of the layer. We also noted that in the literature [3], GaN that was initially facetted would result in VTDs turned to horizontal when followed by lateral growth. We therefore developed a sequence of growth steps to produce GaN growth on narrow mesas with facets. These ideas formed the basis for a first successful attempt to improve on Cantilever Epitaxy and achieve further reductions in VTDs.

Both schemes reduce VTD density at the top of the GaN, and if done correctly, the facetted turning is especially effective. Further, when narrow mesas are used, a greater fraction of area at the top of the GaN is over trenches and is relatively dislocation free, giving a lower overall VTD density. But wider cantilever spans require greater growth times, as does forming facets on GaN over the mesas. The exact growth scheme must then be carefully timed so that lateral growth and coalescence of the cantilevers is completed before unwanted GaN growing vertically in the trenches encounters the cantilevers and introduces numerous additional dislocations. A significant processing accomplishment that allowed greater freedom in developing growth schemes was improving the patterning and etching of the trenches to obtain a trench depth of ~3 μm, allowing greater time for manipulating cantilever growth.

Growths of CE-GaN were carried out on a variety of mesa widths with and without a facetted growth step. Many VTDs were found to turn to horizontal, but many also remain vertical when no facetted step was used. The number remaining vertical varied between observations, but was usually in the range of 30 -70%. When a facetted growth step at 950°C of GaN over the mesa was included in the sequence, the fraction of VTDs remaining vertical was further reduced and depended on mesa width. This successful advance of CE growth methods was published in Applied Physics Letters [4].

In this initial investigation, nucleation of the nitride structure on the sapphire was done with an AlN nucleation layer, which in growth on planar sapphire (no CE) produces a VTD density of ~$2x10^9/cm^2$. With the VTD turning methods just described, the VTD density at the top of the GaN layer was reduced to $3 – 8x10^7/cm^2$, averaged across broad areas that included several mesas and coalescences. This represents a reduction in VTD density achieved with cantilever epitaxy of ~1/40 relative to planar growth.

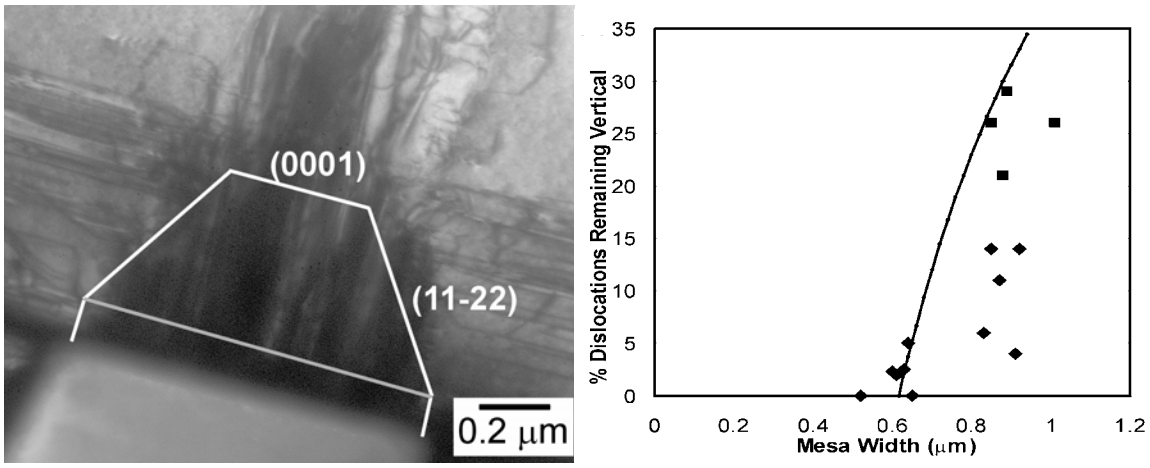

(a) **(b)**

Figure 2. (b) XTEM Bright-field, (11-20) image showing the fraction of VTD turning depends on the mesa width. Mesa width is 1.0 μm. The outline shows the facet structure expected to have formed during the initial vertical growth. (b) The percentage of VTDs remaining vertical is plotted versus mesa width. The curve is the fraction of mesa area not covered by {11-22} facets.

Implement Inherently Low-VTD GaN Nucleation Layer

To reduce VTD densities further, we implemented a GaN nucleation layer to CE growth. This nucleation method was developed to reduce VTD density for planar growth on sapphire by delaying the transition from the nucleation layer with its facetted island morphology to the smooth, planar growth at high temperature [5]. In planar growth, this scheme produced a reduced dislocation density of $5x10^8/cm^2$. When this delayed-nucleation method was used to nucleate GaN on mesas for CE growth that included faceting for VTD turning, a broad-area VTD density of $2\text{-}5x10^7/cm^2$ was achieved for a reduction factor of ~1/12.

To assess VTD densities at the top of the GaN layer, we used a combination of AFM, scanning cathodoluminescence (CL), and plan-view TEM. To obtain accurate VTD counts a collage of plan-view TEM images extending across several cantilever periods was produced. To create such broad-area TEM images, special methods were developed for back-thinning the specimen through the sapphire substrate [6]. In CL, the VTDs reaching the surface appear as dark spots where the luminescence is quenched around the dislocations. With CL, even larger areas can be scanned readily using an SEM; this method gave the range of densities noted immediately above using observations between several areas and specimens grown with the special GaN nucleation layer and the same CE growth details. The dark spots directly indicate why it is important to reduce VTDs: the dislocations are centers of non-radiative recombination of electrons and holes in GaN and in the active layer of LEDs that would be formed at the top surface.

Elimination of Dark-Block Defects

As we developed the CE growth methods described in A (narrow, facetted mesas) and B (GaN nucleation layer) above, our material apparently became more susceptible to a new type of structural defect. We labeled these "dark-block defects" because the defect appears as a dark, non-radiative rectangular block when observed by CL (see Fig. 3). Cross-section TEM showed that these defects are produced when misoriented cantilevers are grown together, which produces a crack between the cantilevers. Plan-view TEM showed dislocations bowing out along the crack line and radiating outward from voids at the ends of the crack [8]. High magnification CL images confirm that TEM is indeed examining the same defects by

resolving individual dislocations bowing outward from the centerline. Clues to the inherent cause of these defects were discovered through close examination of cantilever growths that were halted before coalescence. SEM images indicated that during cantilever growth, sections of material had developed that were tilted just as found with cross-section TEM. The perspective cross-section SEM images also showed the void at one end of the defect and the crack between the cantilevers. They also showed that when the two tilted sections are grown together, the higher side overgrows the lower. This produces a surface relief that can be detected with optical microscopy and corresponds in shape and position with the dark, non-radiative areas seen with CL. All this information together indicated that the problem was with the initial growth of cantilevers and with the way they are grown together at coalescence.

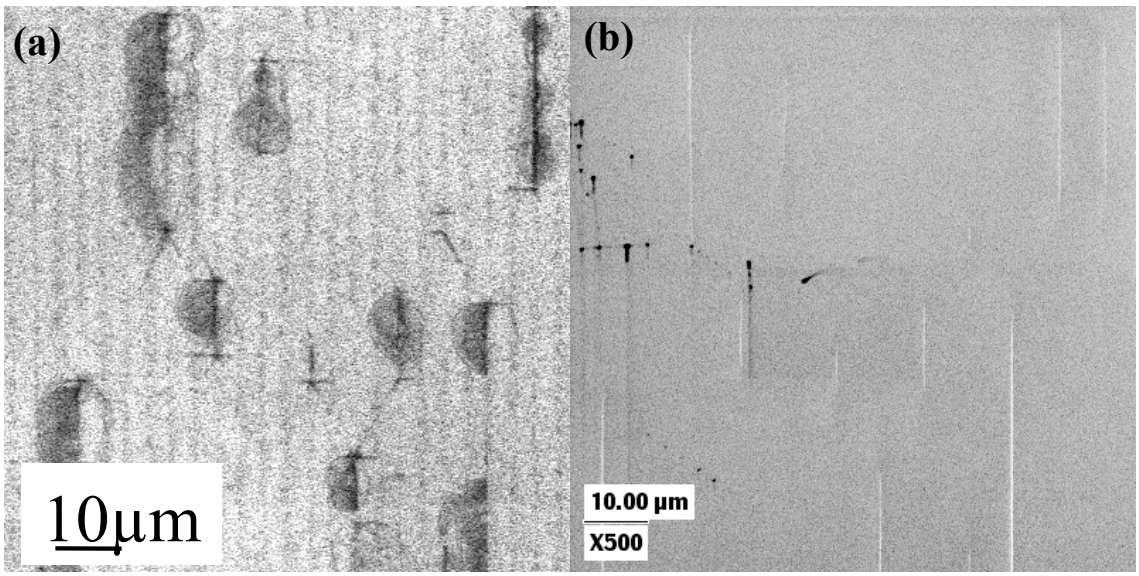

Figure 3. (a) (left) Scanning CL and (b) (right) corresponding SEM image of CE-GaN in an area showing dark-block defects. Image (b) is slightly shifted from (a), but shows a one-to-one correspondence of bright-contrast ridges on the centerline of each dark defect in (a). Note that dark circular loops are resolved at some defects in (a), indicating that dislocations are present and have lateral line segments lying in the growth plane.

We found that two modifications to our CE growths were able to eliminate dark-block defects [9]. First, the initial nucleation of GaN on the mesas needed to be fully dense. This was accomplished by growth to a fully developed, completed "gable" structure composed of two {11-22} crystal facets when the nucleation is done at 500°C instead of 550°C. This well developed structure reduces the tilting of subsequently grown cantilever sections. Second, we found that when the cantilevers are grown together with reactor conditions producing {11-22} facets at their edges, all of the dark-block defects could be eliminated. With these two modifications to our growth methods, non-radiative dark-block defects were eliminated.

Methods to Count Dislocations Accurately

Atomic force microscopy (AFM) and cathodoluminescence (CL) were routinely performed on relative large areas for dislocation counting. Reasonable agreement between the two techniques was obtained by "round-robin" testing of layers at both Lumileds (AFM) and Sandia (CL). AFM images of typical standard and CE InGaN/GaN layers is shown in Fig. 4, showing the significantly reduced dislocation density for CE. The trend in dislocation density reduction throughout the program, by employing improved techniques mentioned above, is shown in Fig. 5. These numbers determined by AFM and CL were corroborated with TEM, as described below.

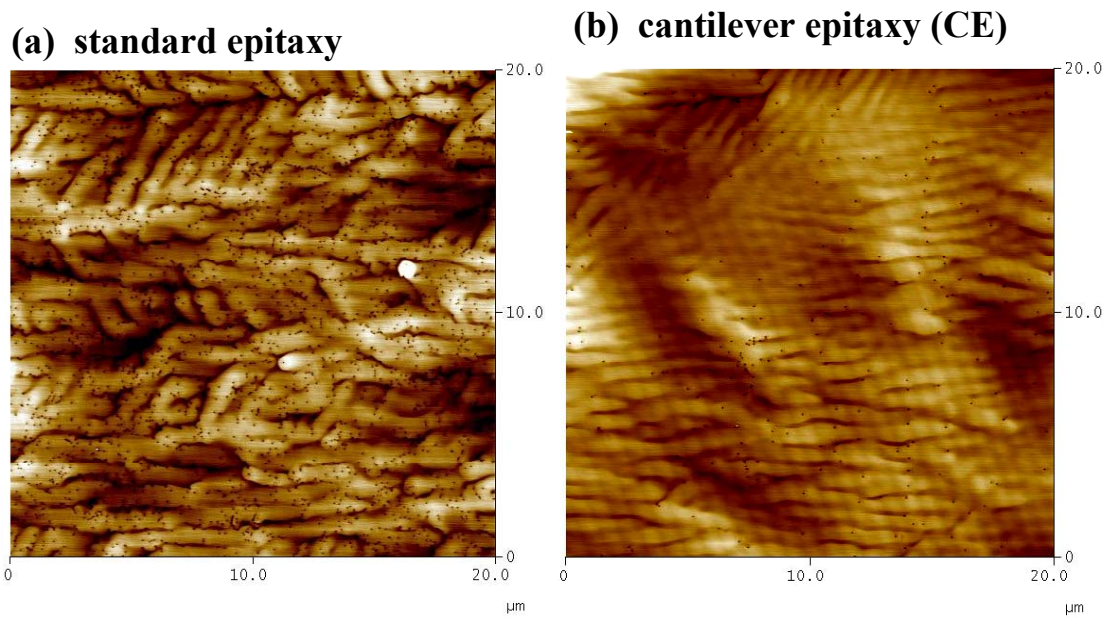

Figure 4. Atomic force micrographs of an InGaN/GaN multiple-quantum-well structure grown on (a) standard, and (b) cantilever epitaxy (CE) GaN layers, exhibiting the strongly reduced dislocation density for CE material.

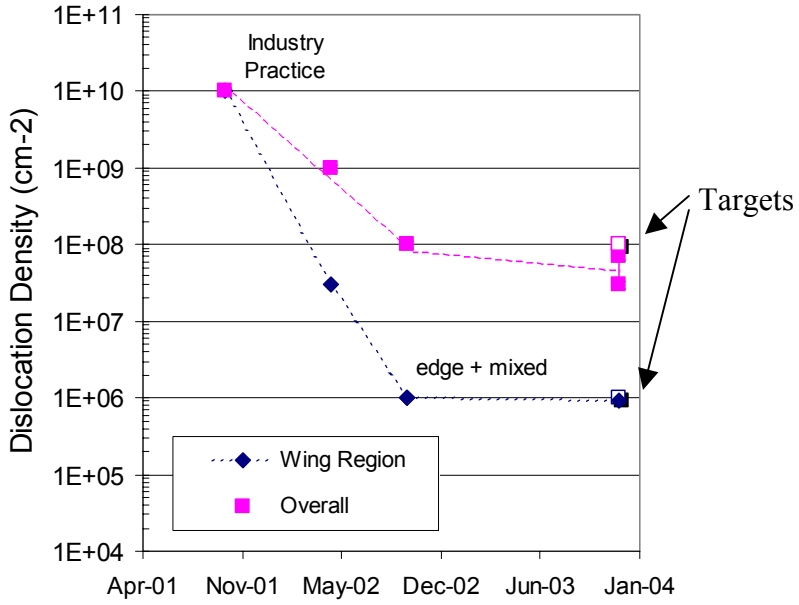

Figure 5. Evolution of progress in threading dislocation density (TDD) reduction in cantilever epitaxy achieved during throughout the program. The final targets of TDD of 1E6 cm^{-2} in the wing region and 1E8 cm^{-2} overall were met.

TEM is generally accepted as the most accurate method to detect dislocations reliably, although it is limited to the small areas of the growth surface thinned for electron penetration. However, in the case of VTDs, discussions in the literature and with colleagues working with GaN suggested that screw dislocations, which have Burger's vector **b** = **c** (where **c** is the crystallographic unit displacement along the hexagonal axis) might go undetected. This was thought to be so because the widely used criterion for TEM dislocation contrast, **g●b ,** is zero when imaging with diffraction vector **g** in the basal plane of the hexagonal crystal. With this criterion, the other two dislocation types, edge with **b** = **a** (**a** is the crystallographic unit displacement in the basal plane) and mixed with **b** = **a** + **c**, should be detected.

However, Sandia demonstrated that a second contrast mechanism produced by strain relaxation around screw dislocation cores that intersect a free surface also operates. We identified an imaging method that allows all three dislocation types to be detected at once; moreover, it allows the type (screw, edge or mixed) of individual dislocations to be determined from their contrast. This identification of the three types is demonstrated in Fig. 6. In a rather dramatic reversal from the expected contrast, screw dislocations show strong contrast and are readily detected, whereas edge dislocations show weaker contrast and require careful imaging to detect. Our imaging methods and the demonstration of dislocation identification were published in Ref. [7]

We also developed methods to prepare TEM specimens with larger thin area for observation. These used special polishing wheels as discussed in Ref. [6]. These preparation methods produced the extended thin area for assessing dislocation densities. We used the contrast identification method to determine the percentages of the three VTD types: screw: 22%, edge: 14%, mixed: 64%.

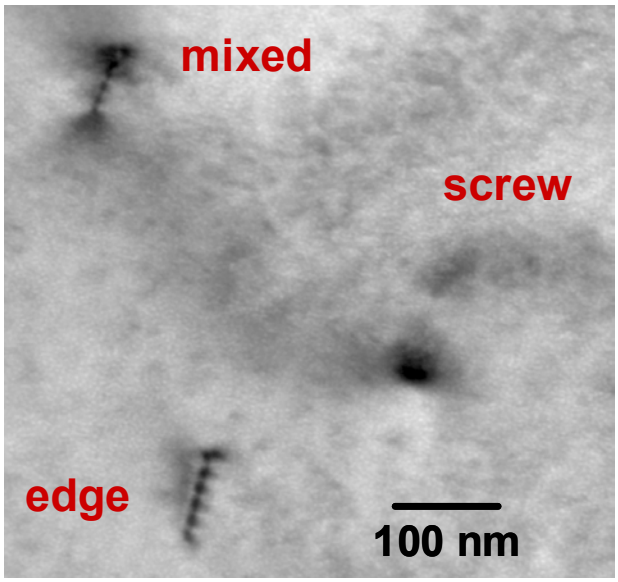

Figure 6. Image demonstrating that all three VTD types can be detected and identified in plan-view TEM [7].

I-C. Device Layer Characterization

Of primary interest regarding the Cantilever Epitaxy (CE) films with their lower threading dislocation density are the electrical and optical properties which could impact performance in LEDs. During Year 1, we focused on simple layer structures rather than full LED structures, in order to systematically study the impact of dislocation density on device performance. To that end, we studied GaN:Si, GaN:Mg, and InGaN/GaN quantum well heterostructures (QWHs). In order to have a direct comparison with standard (non-CE) material, each layer was grown *in the same epitaxial growth run, simultaneously on both standard and CE starting GaN layers*.

Electrical Properties (GaN:Si and GaN:Mg)

The electrical properties of both n-type GaN:Si and p-type GaN:Mg layers, grown on standard and CE starting GaN layers were investigated. The electrical properties were determined using Hall measurements, where we quickly found that an isolation layer was necessary to electrically isolate the upper layers from parasitic transport in underlying layers. Using isolation junction layers (GaN:Mg followed by GaN:Si) beneath, we were able to decouple the transport characteristics of the uppermost GaN:Mg layer on CE material. The layer structure and Hall data are summarized in Fig. 7. We measured a room-temperature mobility of ~9 cm^2/Vs on CE, compared to ~10 cm^2/Vs for standard material. [check xxx] The comparable values suggest that while CE provides no significant enhancement to the transport characteristics, neither does it induce a penalty. For GaN:Si layers, a first attempt with a GaN:Mg isolation layer was not successful, and data indicate measurable contribution from parasitic conducting layers. So, direct comparison between CE and standard epitaxy were not possible for the GaN:Si layers. We will attempt to revisit this issue in Budget Period 2.

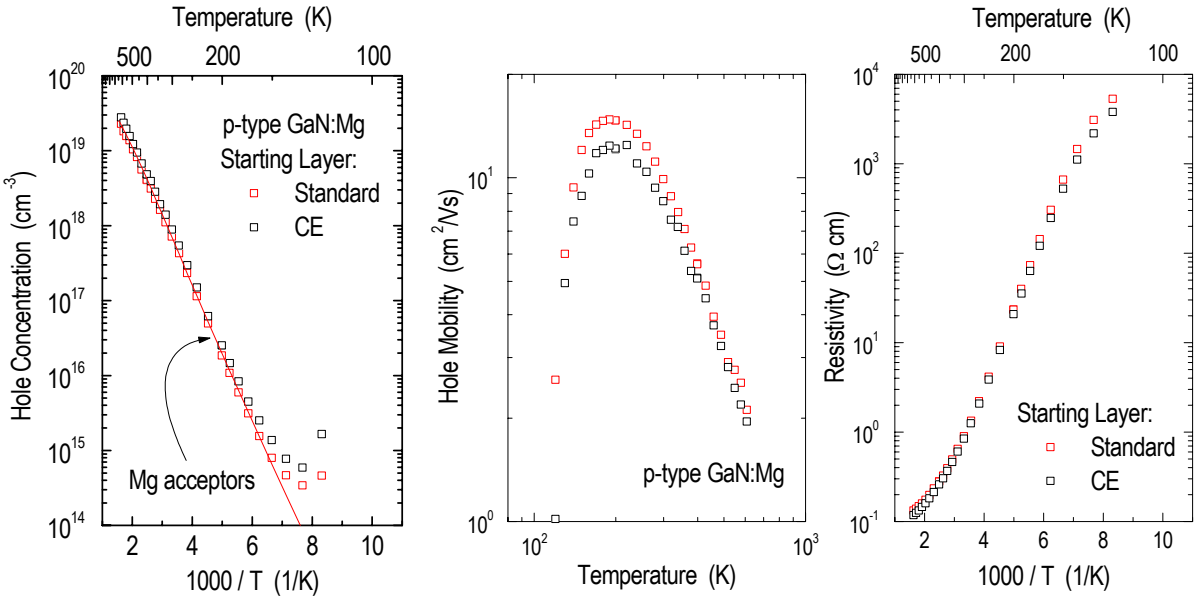

Figure 7. Variable temperature Hall measurement data for GaN:Mg layers on standard and cantilever epitaxy, with an isolation junction in between. Shown are (a) hole concentration vs. inverse-temperature, (b) hole mobility vs. temperature, and (c) resistivity vs. inverse-temperature.

Optical Properties (GaN:Si, GaN:Mg, and InGaN/GaN Quantum Well Heterostructures)

The optical properties of GaN:Si, GaN:Mg, and InGaN/GaN QWHs grown on standard and CE starting GaN layers were investigated. The optical properties of GaN were measured using a pulsed N_2 laser (~ 1ns, 337 nm). The optical properties of the InGaN/GaN were measured using direct excitation of

the quantum wells using a long pulse-length laser diode (405 nm). All measurements were performed at room temperature.

The results for the GaN:Mg and GaN Si layers are shown in Fig. 8. For GaN:Mg layers (Fig. 8a), the direct comparison between CE and standard epitaxy was difficult due to short lifetimes for both layers. While both lifetimes are near the resolution limit (< 1 ns), the CE layer exhibits ~ 2x more light output than the standard layer. More striking results were observed for the GaN:Si layers (Fig. 8b). GaN:Si on CE exhibited brighter luminescence (~2x) and significantly longer lifetime (~2.8 ns) compared to GaN:Si on standard epitaxy (<1 ns). The decay of the standard GaN:Si layer is near the resolution limit of the system (~ 1 ns), so the lifetime may in fact be much shorter. Because the doping levels of the two layers are the same (same growth run), the observed increase in brightness and lifetime for CE indicate reduced nonradiative centers in GaN:Si compared to standard epitaxy. While a portion of the brightness gain may be due to increased light extraction from CE structural features, the increase in decay time is direct evidence of improved material quality.

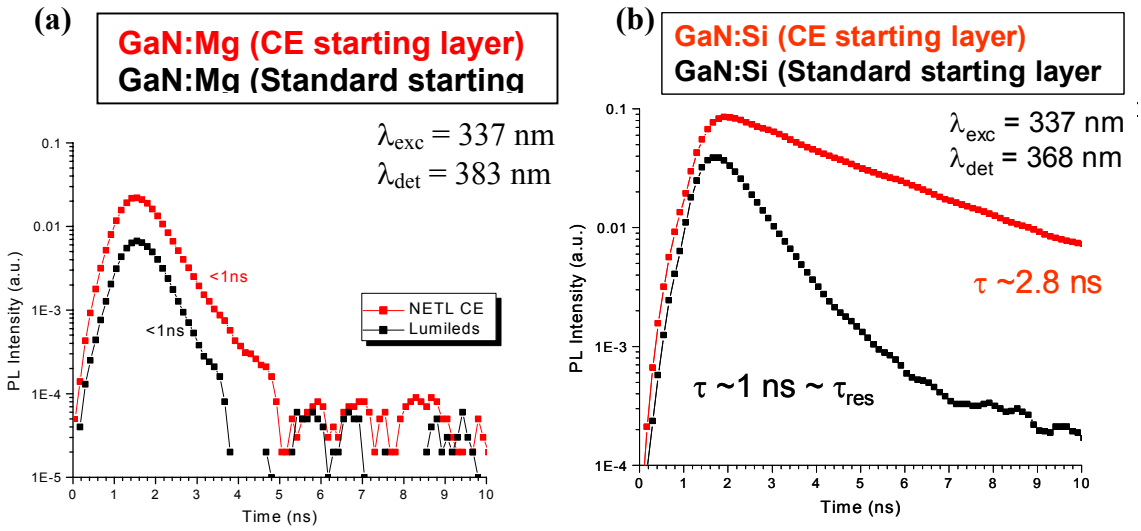

Figure 8. Integrated emission decay characteristics for (a) GaN:Mg and (b) GaN:Si layers grown on both standard and cantilever epitaxy starting layers. The excitation wavelength was 337 nm and the resolution limit of the system is about 1 ns.

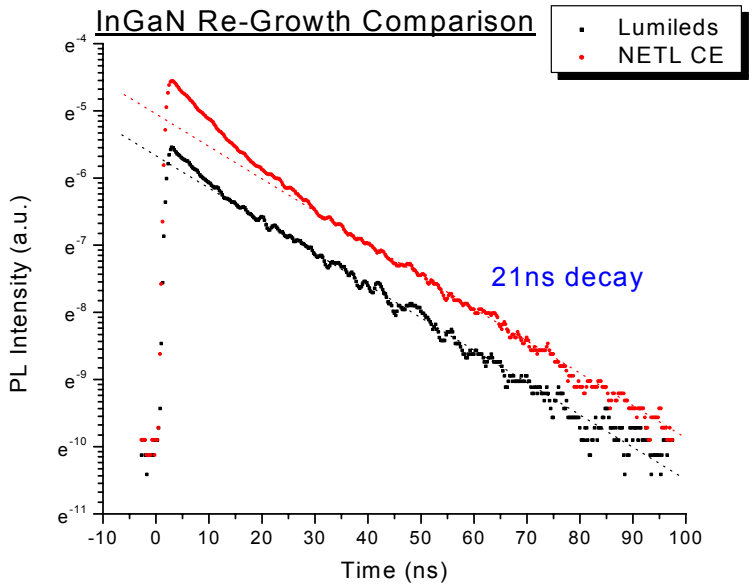

Figure 9. Integrated emission decay characteristic for an InGaN/GaN multiple-quantum-well structure grown on both standard and cantilever epitaxy starting layers. The excitation wavelength was 405 nm (direct excitation of the quantum wells) and at low excitation level.

InGaN/GaN QWHs were studied using direct excitation of the quantum wells. This technique avoids surface and diffusion-related effects and most directly assesses the quality of the quantum well material. The InN mole fraction in this structure was chosen to provide blue emission at ~ 450 nm. The emission and decay characteristics are shown in Fig. 9. For the low excitation density employed, very long lifetimes of ~21 ns were observed for both standard and CE structures. The brightness gain for the CE layer is presumed due to light extraction effects. These results suggest that at low carrier densities, the difference in dislocation density does not affect the optical properties of the InGaN quantum wells. The observation is consistent with the model of InN compositional fluctuations acting a localization centers for electron-hole pairs. Further work will investigate the comparison of low and high TDD regions under higher excitation levels and at elevated temperatures, comparable to typical operating conditions for LEDs. Also, the effect of InN mole fraction in the quantum wells will be investigated by fabricating and characterizing InGaN/GaN MQW structure of varying emission wavelengths.

I-D. LED Characterization

Epitaxial growth

All epi structures characterized at Lumileds in this report are listed in TABLE III. The starting layers were split into half wafers or quarter wafers and placed in the reactor for regrowth of LED layers in the same growth run, for direct comparison of the effects of the starting layer on LED performance, whether cantilever epitaxy (CE), standard, or two-step ELOG (one run only).

TABLE III: SNL and Lumileds epi IDs linking CE and standard GaN staring layers to regrown devise structures. Average PL and EL wavelengths are included.

Substrate ID	Starting Layer	Regrown Layer	PL Wavelength	EL Wavelength	Lumileds epi ID
DSP18-CV2724	CE	Structure F	465 nm	456 nm	RD3020826D
KC-007-091	Standard	Structure F	444 nm	439 nm	RD3020826D
DSP18-CV2724	CE	Structure F	435 nm	428 nm	RD3020905H
KC-007-092	Standard	Structure F	420 nm	417 nm	RD3020905H
DSP60-CV3019	CE	Structure F	405 nm	408 nm	RD3030113B
DSP60-CV3019	CE	Structure F	440 nm	448 nm	RD3030113H
KC-011-088	Standard	Structure F	425 nm	439 nm	RD3030113H
KC-011-087	Standard	Structure F	495 nm	493 nm	RD3030114D
KC-011-087	Standard	Structure F	455 nm	435 nm	RD3030114F
KC-013-006	Standard	Structure F	380 nm	381 nm	RD3030714H
DSP -CV3242	CE	Structure F	382 nm	384 nm	RD3030716D
KC-011-065	Standard	Structure F	378 nm	380 nm	RD3030716D
KC-007-049	Standard	Structure F	400 nm	403 nm	RD3030718D
KC-011-060	Standard	Structure F	430 nm	423 nm	RD3030721B
DSP218-CV3333D	CE	Structure F	399 nm	395 nm	RD3030929H
DSP213-CV3345A	CE	Structure F	400 nm	402 nm	RD3031002B
DSP213-CV3345B	CE	Structure F	393 nm	385 nm	RD3031002H
DSP213-CV3345C	CE	Structure F	404 nm	397 nm	RD3031013F
DSP213-CV3345D	CE	Structure F	426 nm	420 nm	RD3031014F
KC-007-050	Standard	Structure F	396 nm	394 nm	RD3031007H
KC-007-050	Standard	Structure F	443 nm	432 nm	RD3031008I
KC-007-050	Standard	Structure F	422 nm	416 nm	RD3031010H
DSP218-CV3333B	CE	Structure G	458 nm	N/A	RD3031201D
ELO-02-008	ELOG	Structure F	417 nm	414 nm	RD3030515F-1

LED structure (labeled as structure F) is illustrated in Fig. 10. Approximately 2 μm thick Si-doped GaN were grown on top of the starting layers. Then, a light emitting region consisting of 4 InGaN QWs and 3 GaN barriers was grown. The InN composition of the QWs was varied to achieve the desired color and ranged from ~5 to ~20 %. The thickness of the InGaN QWs was ~25 Å. The thickness of the barriers was ~120 Å. A 150 Å GaN cap layer, a 280 Å Mg doped $Al_{0.12}Ga_{0.88}N$ layer and a 900 Å Mg doped GaN layer were grown on top of the InGaN QWs.

InGaN containing layers (labeled as structure G) is illustrated in Fig. 11. A 3000 Å thick low-T GaN layer was grown on top of a 2 μm thick Si-doped GaN grown at high-T and on top of the starting layer. The low-T GaN layer was capped with a light-emitting layer similar to structure F described in earlier reports.

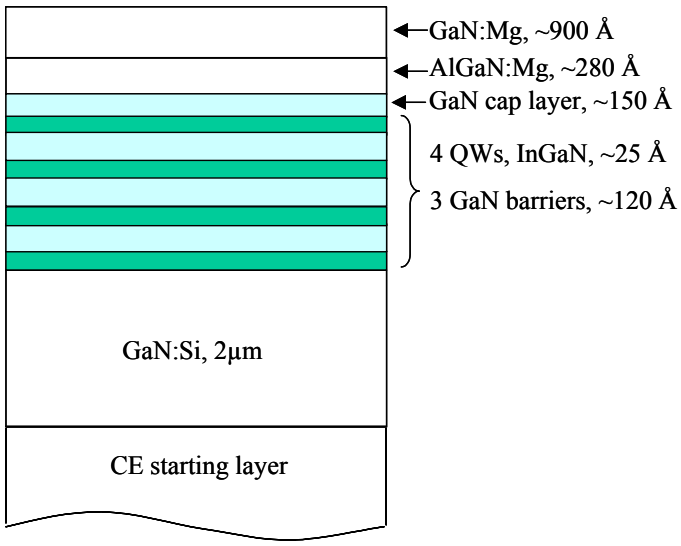

Figure 10 : Schematic of structure F regrown on CE and standard GaN starting layers

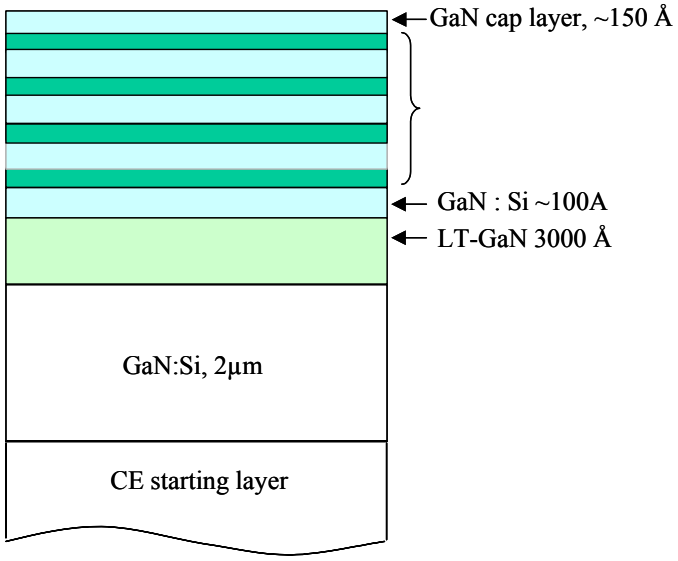

Figure 11 : Schematic of structure G regrown on CE starting layers

LED performance

The external quantum efficiency (η_{EQE}) at 350 mA (pulsed, 2 % DF) and room temperature versus wavelength for the CE, standard, and the ELOG LEDs is shown in Fig. 12. Each data point is for an individual LED. One of the final goals for the project was to show an improvement in external quantum efficiency with LEDs using CE templates. Unfortunately, the data shows that the distributions of the standard and CE LEDs are not much different at 350mA. The η_{EQE} plots similarly for currents of 1A at room temperature. There was a gain at lower currents and higher temperatures (see Fig. 14) that did not translate to higher temperatures or currents. The revealing data points are for the LEDs grown on a double-step ELOG substrate. The total dislocation density for the ELOG substrate is comparable to that of CE starting layers (low 10^7s). However, the η_{EQE} of the ELOG LED is ~28% at 415 nm, well higher than the distribution for both the standard and CE LEDs. The interesting question is why the CE-based LEDs do not fare significantly better than the standard LEDs, with performance closer to that of the ELOG-based LEDs. It is clear that the CE- and ELOG-based LEDs may have extraction efficiencies that are higher than that of the standard LEDs (see Fig.13). In this section we investigate issues related to light extraction.

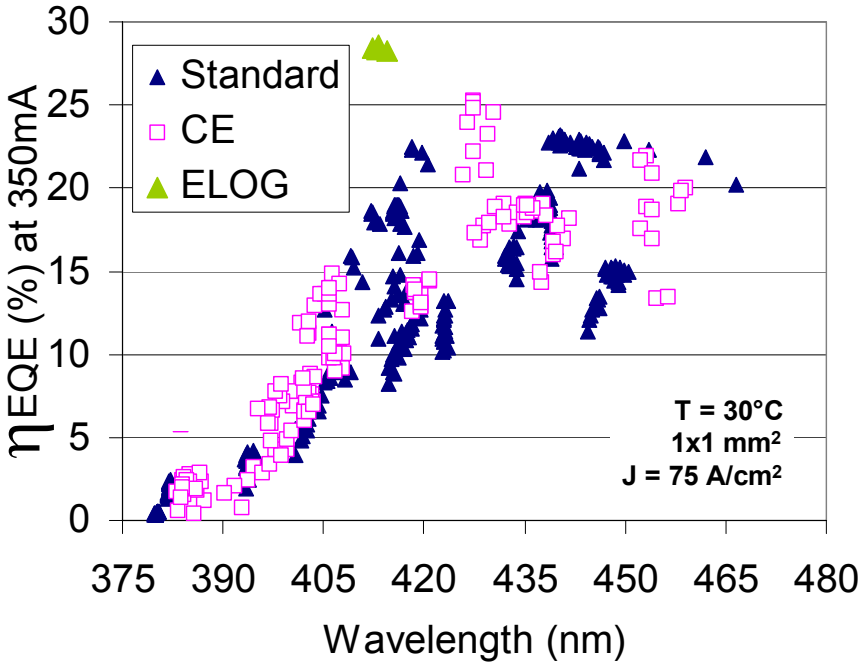

Fig. 12 External quantum efficiency at 350 mA (pulsed, 2% DF) and room temperature versus wavelength for CE, standard and ELOG-based LEDs.

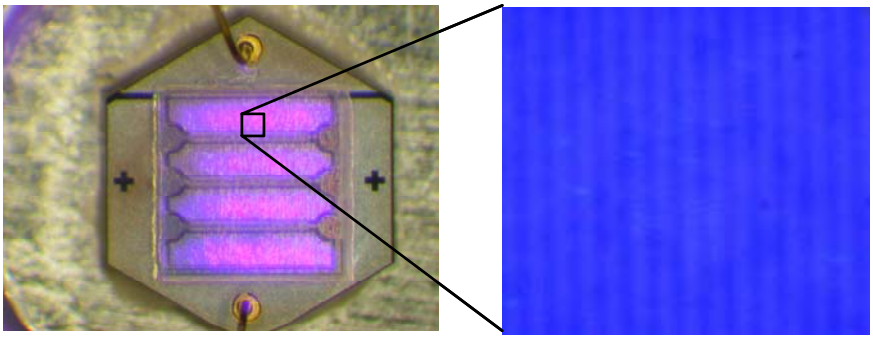

Fig. 13 Photographs of lit CE flip-chip LEDs (full die and close-up). The wing areas appear brighter, presumably due to light scattering.

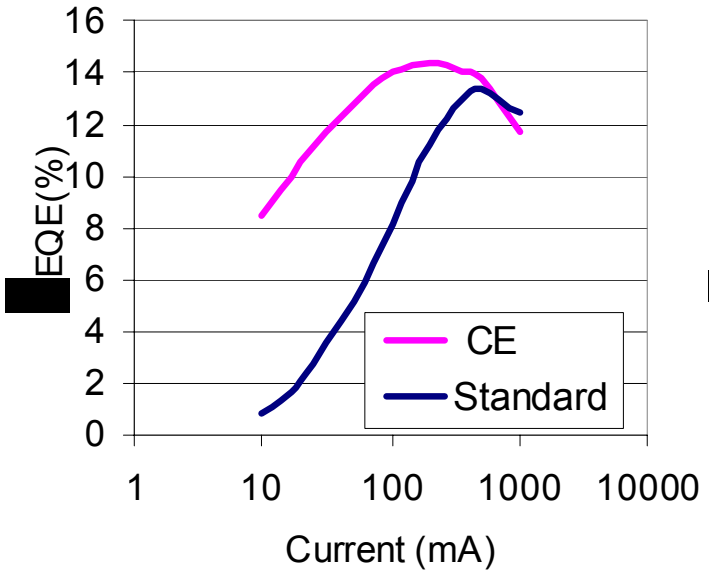

Fig. 14 Typical external quantum efficiency vs. current characteristic comparing standard and CE-based LEDs. The low current performance of the CE-based LEDs is far superior to the standard, suggesting reduced number of non-radiative centers. However, at high currents the performance of the standard LED becomes comparable to that using CE.

Light extraction

Since the low current performance for CE is better than the standard LEDs, and light scattering because of grooves in CE should provide the same or better light extraction, one would expect a net gain in external QE for CE-based LEDs vs standards. One possibility is that the light extraction in CE-based LEDs is compromised. To check this we performed an experiment to measure optical loss (internal absorption) in the starting layers. Samples are placed into an integrating sphere to measure the total absorption in the epitaxial layers. A laser emitting at 458nm is aimed at the sample. Light that is not absorbed by the sample is collected in the integrating sphere. The difference in the input power and the collected power gives the absorption in the sample. The result of measuring a standard LED wafer, a CE template, and an ELOG template are shown in Table IV. As a reference a double-sided polished sapphire wafer yields an absorption of 2% in this set-up. The standard LED wafer has the lowest absorption, but this sample is completely planar so the mean path length of photons in this sample is lower than that of the ELOG or CE samples, which include internal scattering centers (trenches or dielectric ridges). The CE template has the highest absorption. The ELOG also is absorbing significant amounts of 458 nm light. While not a pure quantitative comparison, this measurement suggests that the CE template may have some additional absorption that could reduce the extraction efficiency in CE-based LEDs, compared to the ELOG wafer. This notion is reinforced by the fact that CE starting layers appear more grayish to the naked eye than the ELOG or standard wafers.

Table IV. Measured absorption of a standard, CE, and ELOG-based GaN starting layers.

CE wafer	CE abs (%)	Stand wafer	Stand abs (%)	ELOG wafer	ELOG abs (%)
CV3333a	22.7	RD2030619A	3.3	ELOG1	16.3
CV3333a	18.8	RD2030619A	3.9	ELOG1	16.9
CV3032a	20.7				
CV3032a	28.6				
Average	22.7		3.6		16.6

To investigate what might be the cause of internal optical loss in the CE wafers, we employed fluorescence microscopy, mico-photoluminescence (PL), cathodoluminescence (CL), and bright field (BF) microscopy to further characterize the samples. In particular, we focused on "white/black defects" observable in LED lamps made from CE material. A "white /black defect" shows up as mottled white segment regions when viewed through the sapphire in brightfield and as corresponding dark segment regions when viewed in electroluminescence (EL) imaging through the sapphire. No such defects are found in LED lamps made from non-CE standard material. An example of this is presented in figure 15 showing a bright field image, a low current EL image, and a high current EL image all taken with a 100x 0.9NA objective. The correspondence between the mottled bright appearing segment regions in brightfield and the dark regions in EL are clear.

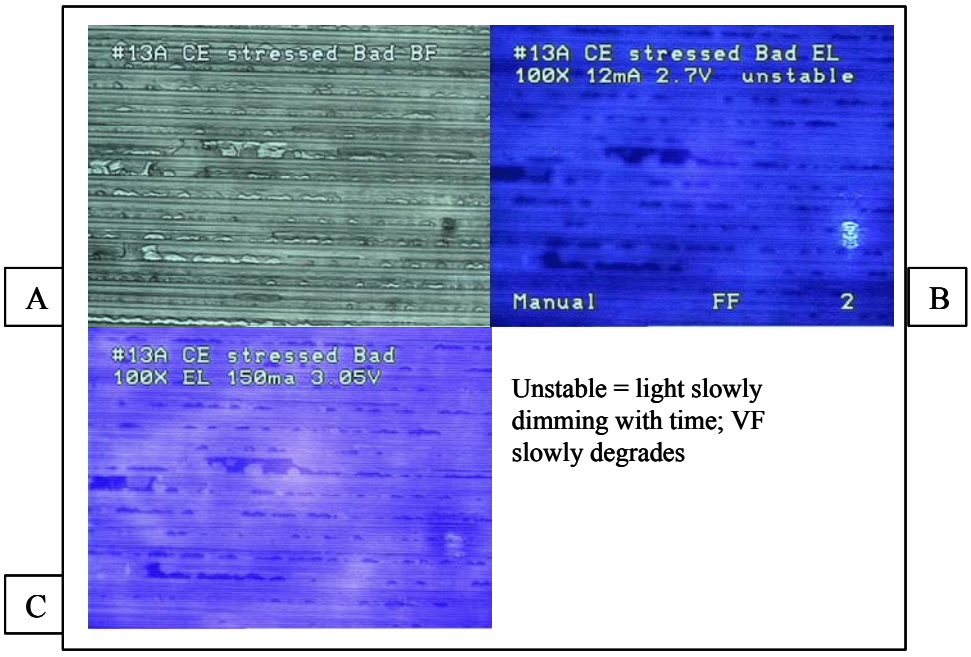

Figure 15. A) brightfield, B) EL low current, C) EL high current, all taken through sapphire with a 100x 0.9NA objective.

In this report we will focus on the photoluminescence results, which are corroborated by micro-fluorescence and cathodoluminescence work (data not shown). When viewed through the CE Sapphire substrate, photoluminescence (PL) and electroluminescence (not shown) are blocked by the white/black defects. Localized PL emission spectral analysis (not shown) confirms that quantum well luminescence is more than 10x dimmer in the white/black defect region (Fig. 16) compared to surrounding "good" areas. On the contrary, viewed on the epitaxial side, the *same* white/black defects are not visible under PL imaging (Fig. 17). It is worth pointing out that these white/black defects also do not appear to influence PL efficiency, as no evidence of non-uniformity in PL around the defects is found (epi side excitation). These same defects are, however, visible under white-light illumination (transmission) in both cases as black (no light) areas, consistent with the occlusion hypothesis.

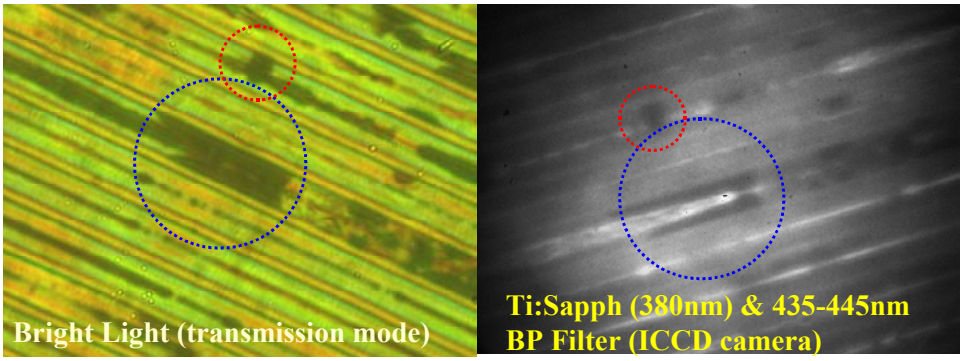

(a) (b)

Figure 16. PL examination through the sapphire at white/black defects with (a) bright light and (b) Ti:Sapphire laser. Both focused on the defect area.

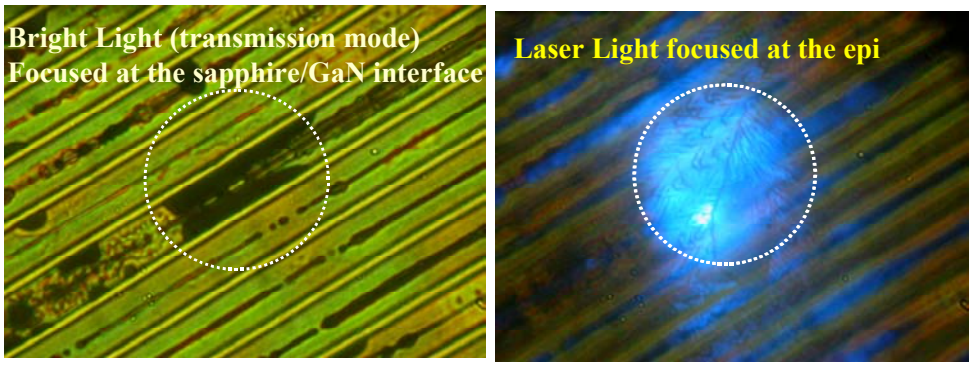

(a) (b)

Figure 17. PL examination through the epitaxial side at white/black defects with (a) bright light and (b) 405 nm laser. Both focused on the defect area.

Although there is scattering from the CE substrate that could increase extraction efficiency compared to the standard LEDs there is also absorption and light blocking occurring in the CE templates. We postulate that the absorption is coming from the GaN deposited in the trenches during CE template growth. In the most extreme cases where white/black defects are present there is also light occlusion also reducing the extraction efficiency of the LEDs. If the internal quantum efficiency is higher in the CE LED wafers as suggested by the hot/cold factors (see previous reports) then this internal quantum efficiency boost is possibly negated by the light occlusion and light absorption present in the CE templates. Also, the absorption and light occlusion loss must be greater than the diffraction gain in the CE templates. Reducing or preventing GaN from growing in the trenches should help prevent this problem.

Light generation

A subset of CE, standard, and ELOG LEDs are measured at 30°C and 120°C at various currents. Figure 18 shows the ratio of η_{EQE} at 120 °C and 30 °C versus wavelength and current (dc) for all of the LEDs measured in the program. This ratio is called a hot/cold factor and characterizes the temperature dependence of the LEDs. The hot cold factor is also an indication of the internal quantum efficiency (IQE) of the LED material as there is typically a good correlation in high current operation. The higher the hot/cold factor the better the IQE. The hot/cold factor decreases as the LED wavelength gets shorter and as the current decreases. Figure 18 shows a difference between the CE and standard LEDs. At wavelengths shorter than 420nm the CE LEDs, on average, have greater hot/cold factors compared to standard LEDs. This is an indication that the reduced defect density is affecting the IQE of the LEDs. What is puzzling is that the ELOG LEDs had the same defect density as the CE LEDs, but the ELOG LEDs have an even better hot/cold factor. There is something limiting the CE LEDs performance.

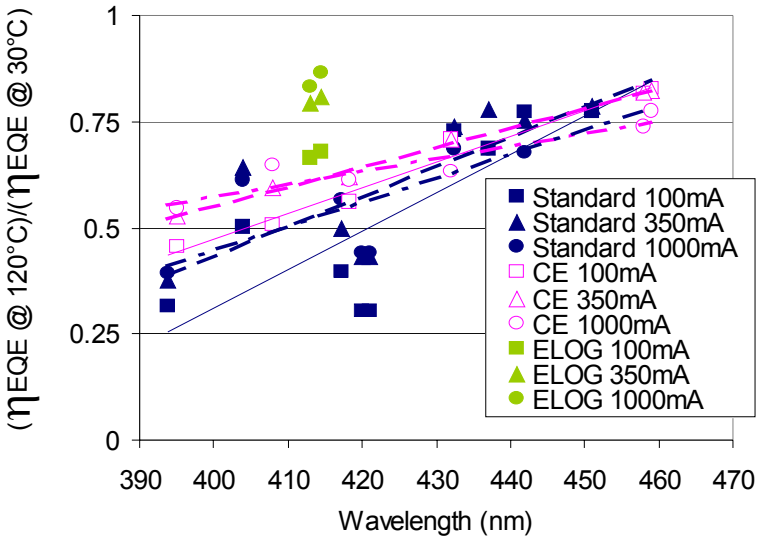

Fig. 18. Ratio of external quantum efficiency at 120C to that at 30C ("hot/cold factor") for several LEDs vs wavelength. Included are standard, CE-, and ELOG-based LEDs.

The next step was to find the location of the leakage on the CE LEDs. We found that not only was the forward bias unstable, but also unstable reverse leakage was present with CE LEDs. Figure 19 shows a typical comparison between good and bad AC curve traces (IVs) for a CE lamp. On standard LED material the forward voltage (Vf) at 1uA is typically 2V and stable (typical for blue LEDs). In leaky CE LEDs the values of Vf at 1uA are far from typical, usually less than 1.4V. There are also differences in reverse voltage (Vr) at –100uA. Good CE lamps Vr is typically –25V and with time moves away from zero by about 10%. Leaky CE lamps start out with a Vr of approximately -25V quickly degrading towards zero. After 2 minutes at -100 uA the Vr value has degraded to below –20V. Unstable behavior can also be seen in Vf at 1uA. Vf at 1uA increases with time after the reverse bias. This behavior was studied with electroluminescence (EL) and reverse biased photoemission (RP) imaging through the sapphire. The location of reverse bias light gives us a possible location for the leakage under forward bias. One standard LED and two CE LED cases are shown.

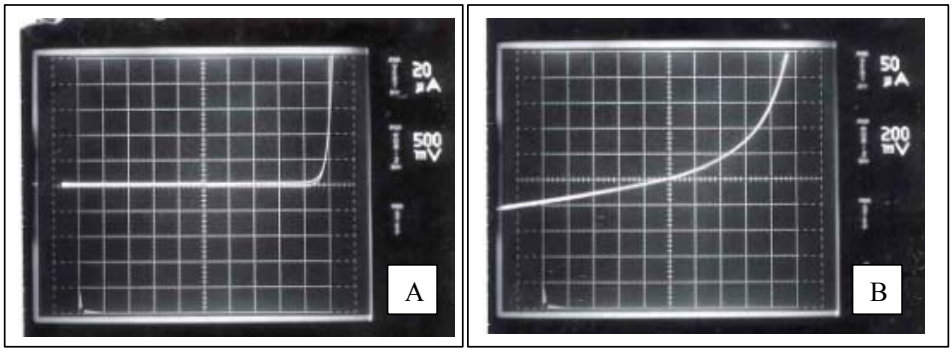

Figure 19. AC curve traces: A) non leaky device CE#10 from R3031014F, and B) leaky device CE#7 from R3031002B.

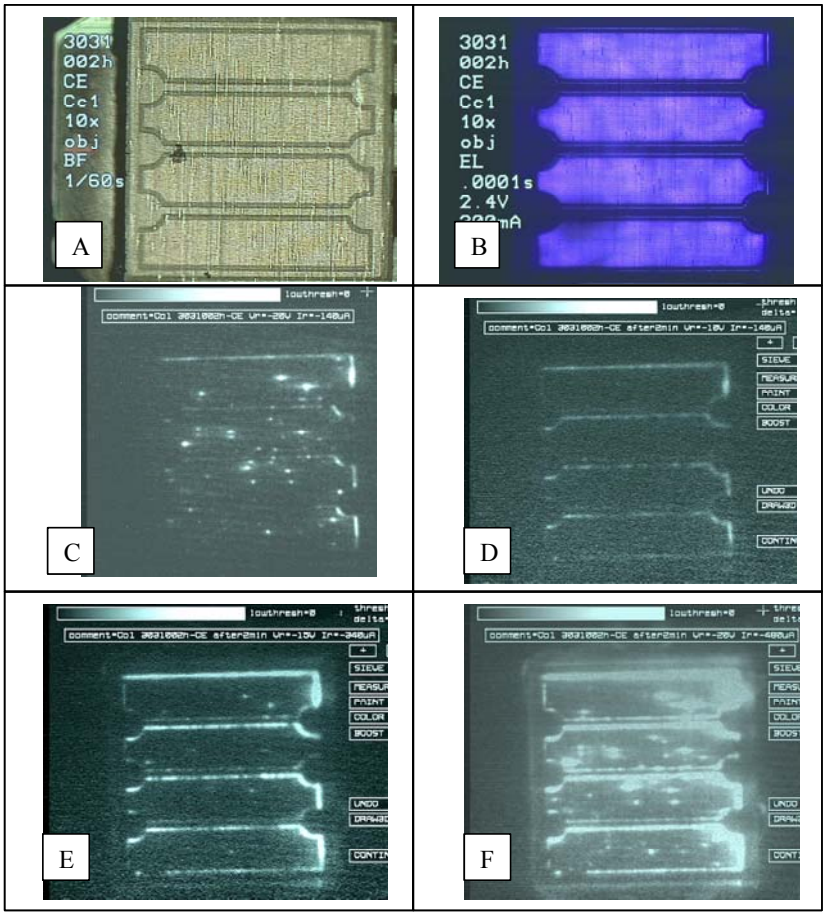

Figure 20. CE lamp #Cc1 from R3031002H: A) brightfield, B) electroluminescence, C) initial reverse photoemission intensity –100 uAVr between –20 and –25V, D) after 2 minutes, -100uA Vr = -10V, E) increasing to –15V now supporting –340 uA, F) increasing to-20V now supporting –480 uA.

A common failure type is represented by CE lamp #Cc1 and CE lamp #Cc9 both from R3031002H. We investigate 2 conditions: 1) Vr behavior without 2-minute forward bias stress and 2) Vr behavior with a prior 2 minute forward bias stress.

EL and RP characteristic of lamp #Cc1 is illustrated by Figure 20 under initial bias. Figure 20.C-D show changes in the RP intensity image with time before forward bias stress. When first reverse biased to –100uA the curve started to collapse toward zero. A quick capture (~10 seconds) between –25 V and –20 V is shown in figure 20C. Along with the familiar RP points we see a strong RP outlining the mesa edge. After ~2 minutes of constant –100uA the Vr has collapsed to –10V and the RP image shows only strong light coming from the mesa edge (figure 20D). From this point increasing the voltage to support higher current we can return the RP points found in our initial image albeit with much more intense edge light (E and F). We conclude that the additional -380uA at -20V is caused by the developing edge leakage. This same behavior was observed in other CE-based LEDs.

The hot/cold factors and improved ideality factors in the CE LEDs suggests that there is improvement in IQE compared to standard LEDs. While the CE LEDs display leakage current, it is unclear that the magnitude of the effect is enough to appreciably reduce IQE at high currents. The leakage current increases with reverse bias and directly correlates to light being generated on the edges of the LED mesas under reverse bias. This is unusual IV leakage behavior and would require additional work to gain insight for proper interpretation. It is our theory that the RIE used to define the p-mesa is adversely interacting at the wing coalelesance regions creating a leakage path, possibly where the wing regions close off (suture). If the suture is not atomically closed-off dry etching could reveal it opening the wing and a potential leakage path. This could be avoided by making sure that the wing sutures are completely closed-off by growing thick coalelesance layers before the n-layers are grown. Also it may be possible that other etch conditions or chemistries could be used to avoid this leakage. While not clearly an effect on IQE, the excessive leakage and poor forward stability of most of the CE-based LEDs would likely result in performance degradation over time, and a solution would be required for CE-based epitaxy to be suitable for industry.

CE lamps were selected for Infrared Thermal Analysis at an outside contractor. The equipment used was QFI InfraScope that incorporates an Indium Antimonide detector and claims 2.8 um spatial resolution and 0.1 degree C temperature sensitivity. The experiment was designed for differential thermal imaging (i.e. hot spot detection). Leaky CE lamps cc5, cc9, ce7 and non-leaky CE lamp ce10 were analyzed together with a non-leaky non-CE device. In summary all the leaky CE lamps showed hot spots at the mesa edge; where as, non-leaky lamps showed a uniform temperature across the die. The hot spots thus correspond to the leakage observed in reversed-biased photoemission measurements. Typical examples are presented in the following Fig. 21: leaky CE lamps cc5 and cc9, and non-leaky CE lamp ce10.

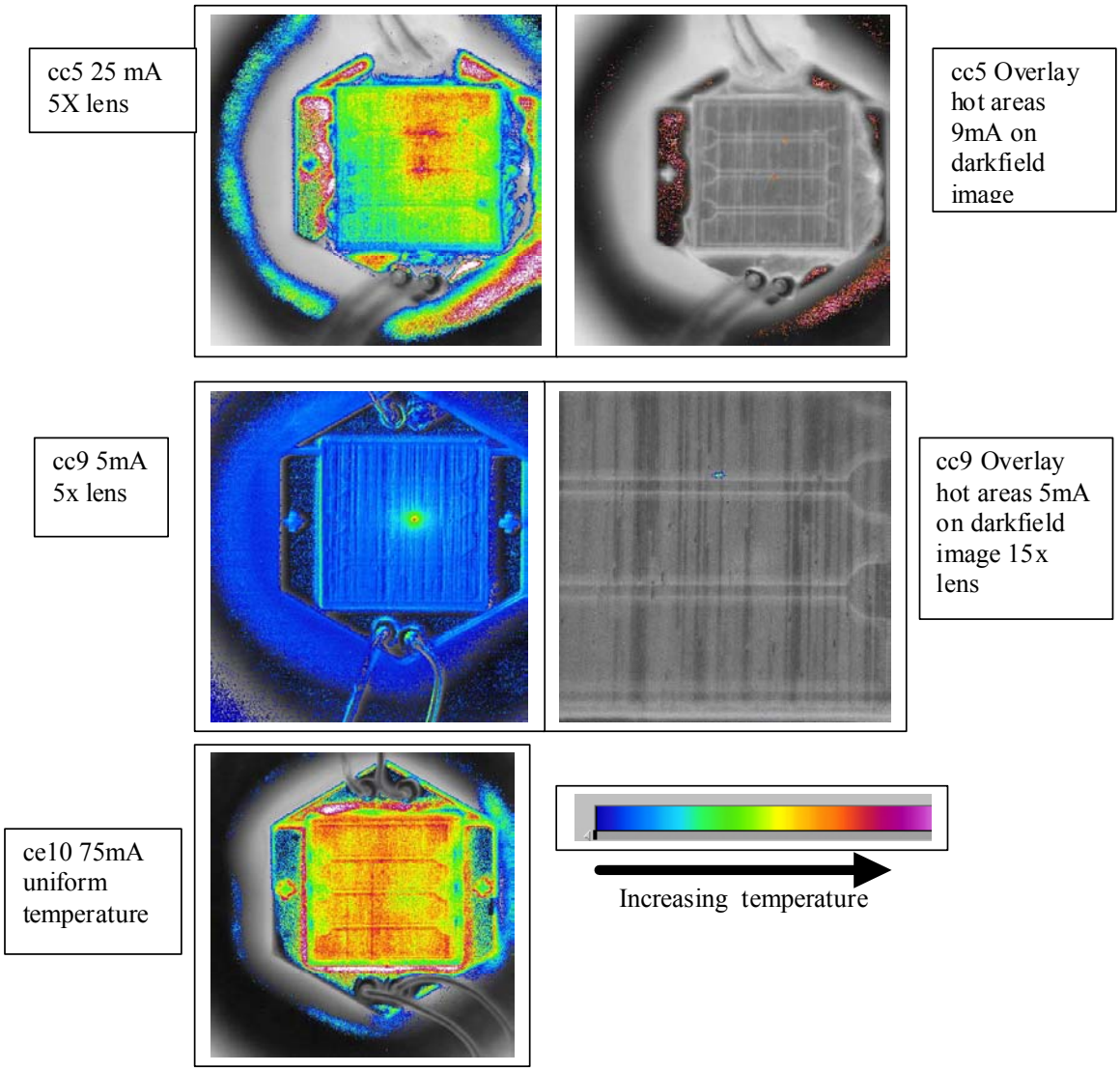

Figure 21. Thermal (left) and reverse-bias photoemission (right) images of CE-based LEDs. The majority have hotspots in forward drive that often correspond with leakage paths in reverse bias.

Conclusion:

Detailed characterization of high power LEDs were performed, comparing the effect of cantilever epitaxy (CE) based LEDs to standard LEDs, and (for one run) to those grown on an ELOG substrate. Several LED growth runs and related lamp characterization show that, compared to standard LEDs: (1) CE-based LEDs have higher external quantum efficiency (EQE) at very low drive currents, (2) CE-based LEDs have a slightly stronger temperature stability of EQE, (3) at operating currents, EQE of CE-based LEDs are similar, and (4) LEDs grown on an ELOG wafer (one run) achieving similar total dislocation density to that of CE provided LEDs with a significant boost in both EQE and temperature stability. The question is: why do the CE based LEDs not provide significant gains over the standard LEDs?

On-wafer measurements suggest that CE based LEDs should provide higher light extraction than standard LEDs, due to light scattering from voids in the GaN/sapphire between sapphire posts. However, encapsulation gains (a measure of extraction) do not differ appreciably from standard LEDs. With more detailed characterization, we found that material within the trenches (observable in LEDs and termed 'white/black' defects in previous reports) is optically absorbing. This is most clear seen in micro photoluminescence images. This observation is reinforced by total optical absorption measurements (458 nm) of CE compared to ELOG starting layers, which show higher loss for the CE starting layers. Presumably, any light extraction benefit that the trenches might have provided, is reduced or even negated by the presence of this optically absorbing material.

We were unable to get a clear picture of internal quantum efficiency (IQE) comparisons of CE vs. standard material. However, strong forward bias instability and resulting forward current leakage are observed for CE-based LEDs. Reverse-bias photo-emission images reveal an abundance of leakage paths associated with the mesa sidewalls of the LEDs, very unusual for standard LEDs. These images correlated well with thermal images taken at forward bias, showing hot spots along the mesa. It is possible that dry etching of the GaN necessary to fabricate LEDs has interacted with partially coalesced sutures to result in increased sidewall leakage, but this is only guess. While it is not clear that the leakage has a significant impact on IQE at high currents, it is certain that this phenomenon would impede manufacturability.

For future work, we recommend that means be provided to inhibit trench/sidewall growth in cantilever epitaxy, e.g. by deposition of passivating dielectric(s), to eliminate poor quality GaN being incorporated into the trenches and acting as optical loss centers, as well as leading to other potential problems. By avoiding this problem, a more clear picture of CE-based LED performance could be realized, and improved estimates of the benefits in external quantum efficiency could be quantified. Furthermore, future work on improved coalescence and device layer growth (e.g., thicker layers) is expected to reduce and hopefully eliminate the electrical leakage problems observed at device mesa sidewalls.

IN SITU TOOLS

II-A. Motivation

The key motivation for this work was to evaluate several different *in situ* monitoring techniques in order to improve the understanding and/or quality of III-nitride metal-organic-chemical vapor deposition (MOCVD). III-nitride epitaxy is complicated by the severe growth conditions (e.g., high temperatures, gas-phase pre-reactions and particle formation) and materials used (e.g., lattice-mismatched, transparent growth substrates). Of particular importance are the gas-phase pre-reactions, which are not fully understood, and a substrate that results in highly strained films and the transparency of which precludes the use of standard pyrometry for directly measuring growth temperature. In this program, we address some of these issues through the development of new tools suitable for use with III-nitride MOCVD, for measuring film composition, strain state, and growth temperature, as well as investigating gas-phase pre-reactions and particle formation during AlGaN growth.

II-B. MOCVD thin film characterization *in situ*

Composition control of III-nitride films is crucial for repeatability and yields of high brightness LEDs. For example, for AlGaN growth by MOCVD, the AlN% incorporation can vary depending on a number of factors, such as trimethylaluminum (TMA) flow to the reactor, growth rate and temperature. Any small deviation in a single parameter can alter the AlGaN film composition. The film composition is measured after growth using *ex-situ* x-ray scattering, however, this slow feedback to any changes in the MOCVD reactor can be costly.

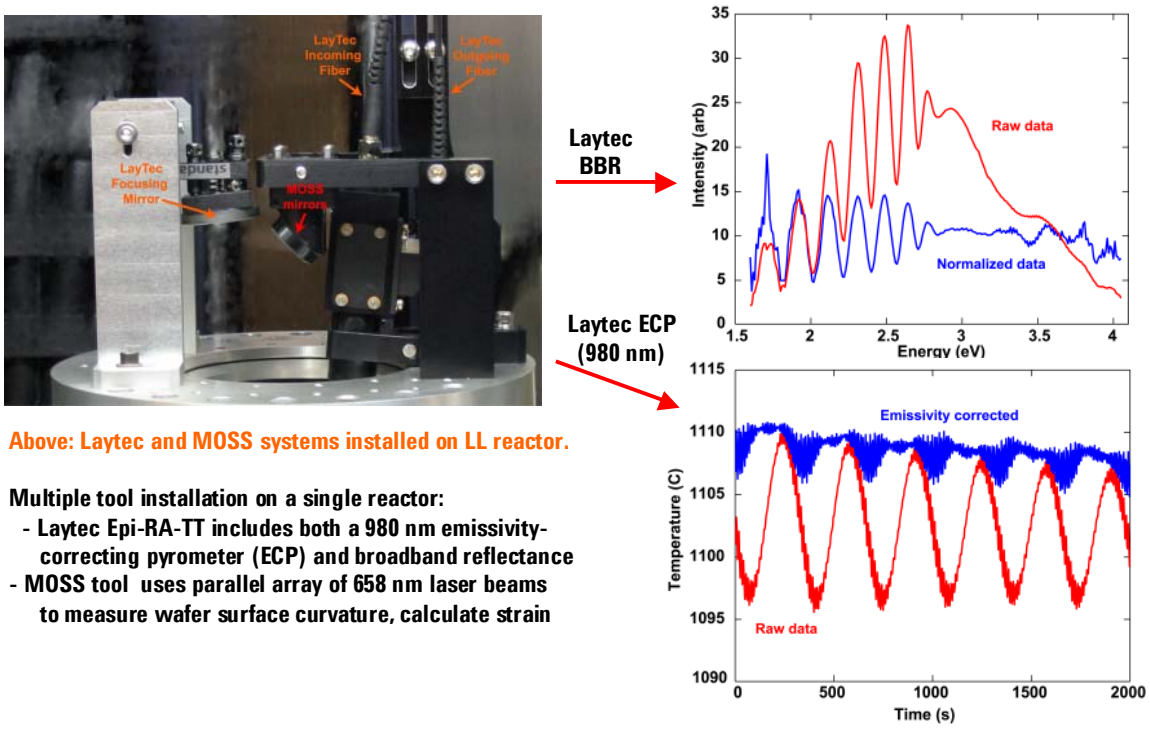

Above: Laytec and MOSS systems installed on LL reactor.

Multiple tool installation on a single reactor:
- **Laytec Epi-RA-TT includes both a 980 nm emissivity-correcting pyrometer (ECP) and broadband reflectance**
- **MOSS tool uses parallel array of 658 nm laser beams to measure wafer surface curvature, calculate strain**

Fig. 22 Hardware configuration (left) and example data for multiple in situ tools installed on a single R&D reactor. Shown are broadband reflectance (top right) and pyrometry (bottom right) data.

The material band gap is a function of the alloy composition, temperature and strain state. Thus by *in-situ* independent measurements of the band gap, the temperature and the strain state, in principle, one should be able to determine the alloy composition of a film during growth. As described in milestone 2.24, we have installed two *in-situ* monitors: LayTec Epi-RA-TT and MOSS, on the same single wafer nitride reactor. The LayTec Epi-RA-TT is a combined emissivity correcting pyrometer and broadband reflectance system, and the MOSS system allows us to measure the wafer curvature during growth, from which the film stress can be determined. The set up (an example data output) are shown above in Fig. 22.

Samples

A series of samples with aluminum nitride target compositions ranging from 0 to 20% were grown. The majority of the samples have the structure shown in Fig. 23, where an AlGaN layer is deposited onto a 0.6 μm thick undoped GaN film on a sapphire (0001) substrate. The AlGaN film thickness varied between 0.3 and 0.6 μm. The thick GaN layer was grown at 1100ºC using trimethylgallium (TMG) as the gallium source with a growth rate of 5.0 Å/s. AlGaN was grown at ~980ºC or ~1135ºC using TMG and trimethylaluminum (TMA) as the group III sources resulting in a growth rate of 0.5-1.1 Å/s. While the GaN was grown in hydrogen ambient, the AlGaN was grown in nitrogen ambient. The switch of ambient was implemented in order to keep the film stable at high temperature during growth pauses for collecting broadband reflectance data with better signal to noise ratio. Film thicknesses were determined using *in-situ* single wavelength reflectance. The aluminum nitride composition of the samples was determined after growth using x-ray diffraction measurements of the GaN and AlGaN 002 reflections. None of the AlGaN films grown for this study exhibited cracks. The bandgap was determined by photoreflectance as discussed in the Y2Q4 report. The results are summarized in Table V.

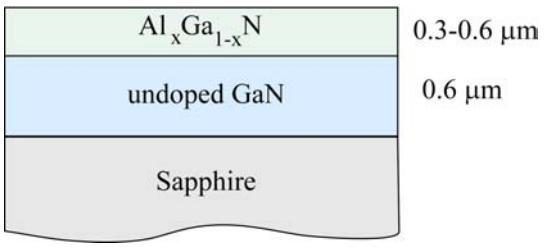

Fig. 23: Schematic of sample structure.

Table V: Description of AlGaN samples. The temperature was measured by the emissivity corrected pyrometer. The AlN% is determined by x-ray diffraction after growth. Band gap measurements of the samples at room temperature were based on PL measurements. (D and E could not be measured, since the laser excitation energy was below the band gap of those samples.)

Sample	Temp (degC)	Thickness (A)	AlN conc. (%)	PL (nm)	Eg (eV)
A	1140	4650	0	362.0	3.426
B	1137	4090	8.28	342.4	3.621
C	1133	3980	11.74	336.2	3.688
D	1135	2950	17.29		
E	1138	3050	19.37		
F	973	5840	4.52	353.0	3.513
G	983	5760	6.67	347.0	3.573
H	980	5820	10.68	339.0	3.657
J	976	3750	13.33	333.0	3.724

Temperature

The band gap dependence on temperature T(K) is often described by the Varshni formula:

$$E_g(T) = E\ (T=0) - \frac{\alpha T^2}{T+\beta}, \qquad \text{(eqn. 2)}$$

The recommended literature values for α and β are 0.909 meV/K and 830K for GaN and 1.799 meV/K and 1462K for AlN [2].

We determined the film temperature using the LayTec emissivity correcting pyrometer that was described in milestone 2.24. As an example, the thermocouple temperature and the pyrometer temperature are shown for the growth of sample C in Fig. 24. While the thermocouple close to the heater is unaffected by process flow changes, the pyrometer is very sensitive. For example as shown in Fig. 24 when then ambient is switched from H_2 to N_2, which is much less heat conductive, the wafer temperature increases by ~40ºC. This is clearly shown in the pyrometer data, whereas the thermocouple (control) temperature does not change. The stepped cool down was used in order to collect broadband spectra as a function of temperature after growth of the AlGaN film for each sample. It is clear that the emissivity correcting pyrometer is superior to the thermocouple for measuring the actual growth temperature.

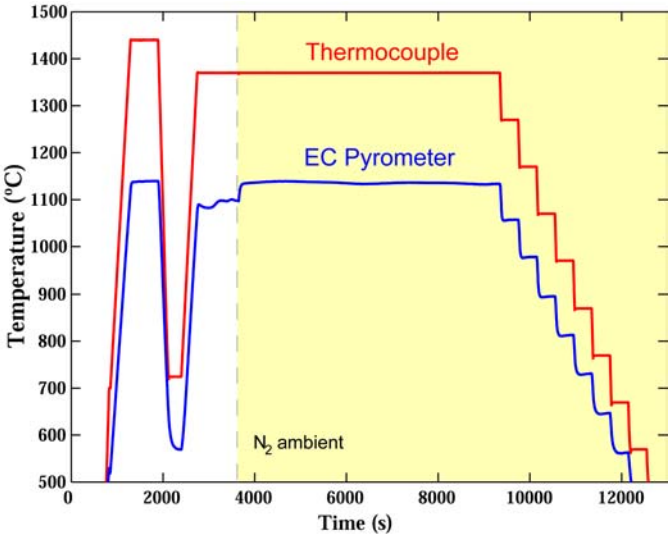

Fig. 24: Thermocouple (red) and emissivity corrected pyrometer (blue) temperature are shown as function of time for growth of sample C. The yellow background corresponds to nitrogen ambient in the reactor.

Broadband reflectance

Using the LayTec system, which is described in milestone 2.24, we collected broadband reflectance spectra during the growth of all samples. In addition, during cooling the spectra were collected at approximately every ~100ºC, as well as at room temperature. The reflectance spectra, which range the energies 1.7-4.7 eV, were normalized to the reflectance spectra of the sapphire substrates. As an example, all the spectra collected during growth of sample C are shown in Fig. 25 as a function of time. The colors represent the reflected intensity.

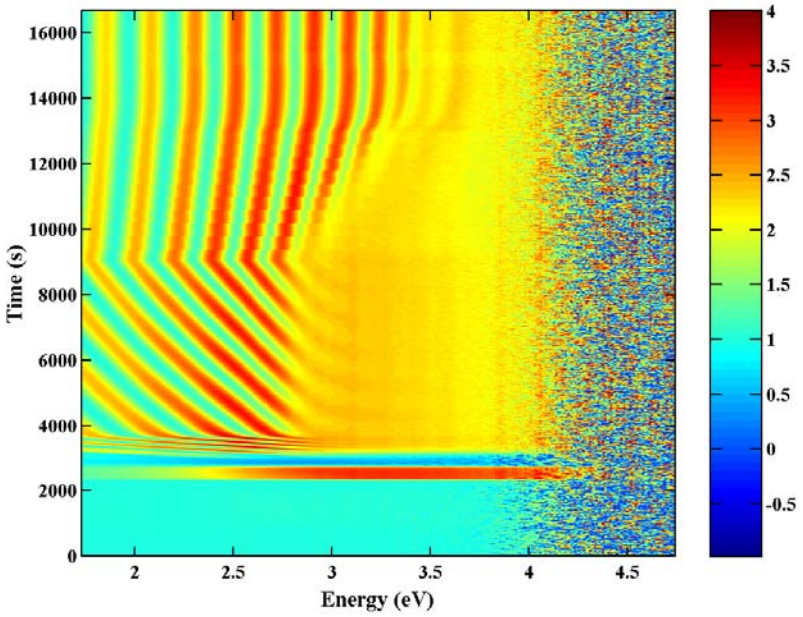

Fig. 25: Broadband reflectance image map for growth of sample C. The intensity is normalized to the reflectivity of sapphire.

In Fig. 25, the maximum of the thickness fringes are shown as intense red stripes. Since the growth rate for AlGaN is ~1/5 compared to the GaN growth, the line width and angle changes dramatically at t ≈ 4000s, where AlGaN growth is initiated on the GaN base layer. Cooling of the sample starts at t ≈ 9000s, where the thickness fringes move to higher energies. While this could be interpreted as negative growth (etching), it is in fact due to the contraction of the GaN and AlGaN films during cooling. In Fig. 25, it is also easily seen that the thickness fringes become visible at higher energies during cooling, which is due to the band gap shifting to higher energy with lower temperature. At energies above 4 eV, noise is dominating the spectra, possible due to UV light being absorbed in the reactor windows.

A broadband reflectance scan was obtained every 5 sec during growth. In order to improve the signal to noise ratio, a series of spectra were also collected at growth temperature during a growth pause, in order to average a series a spectra for the same film thickness and composition. While the band gap is near the point where the oscillations disappear, it is necessary to do further analysis to determine the exact position of the band gap.

Band gap

The broadband reflectance spectra collected at room temperature for film A (0% AlN) is shown in Fig. 26 as the black curve. While the band gap is near the kink in the spectra where the oscillations vanish, the band gap cannot be determined accurately without further analysis. Using AnalysR, which is a software package supplied with the LayTec system, the broadband reflectance can be modeled. The blue curve in Fig. 26 represents the broadband reflectance spectra from a 0.58 mm thick GaN film on sapphire at 25ºC calculated using AnalysR. Note that this reflectivity had to be scaled in order to match that of the data, possible due to roughness of the GaN sample.

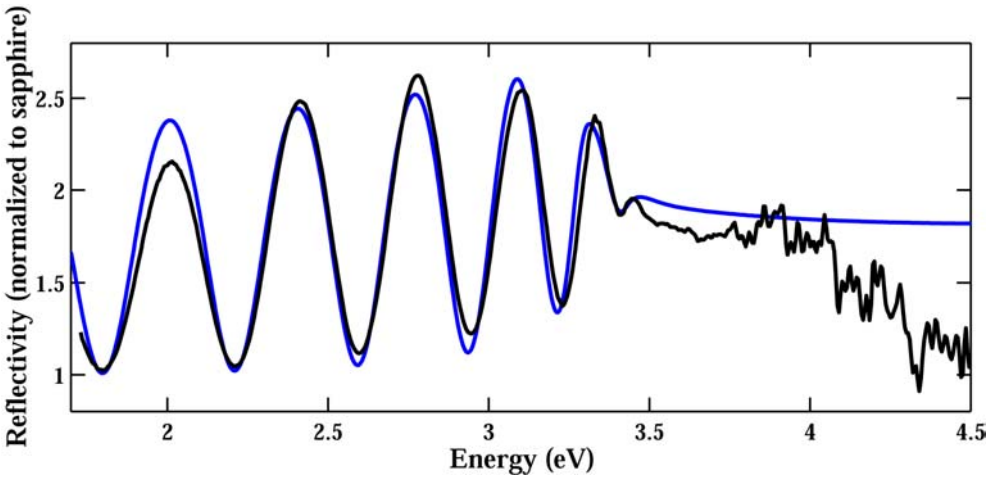

Fig. 26: Room temperature broadband reflectance spectra of a GaN film (black), and simulation of a 5800Å GaN film on sapphire (blue).

The simulation of the broadband reflectance using AnalysR also calculates the optical properties of the film n and k as a function of wavelength. The n and k values for the simulation shown in Fig. 26 are plotted in Fig. 27. The dashed line shows the expected band gap of 3.42 for GaN at room temperature, which also corresponds to the inflection point for the optical constant k. Therefore, if we can calculate a broadband reflectance spectra using AnalysR that is similar to that measured using the LayTec system, we can find the inflection point for the absorption constant k and derive the band gap of the material.

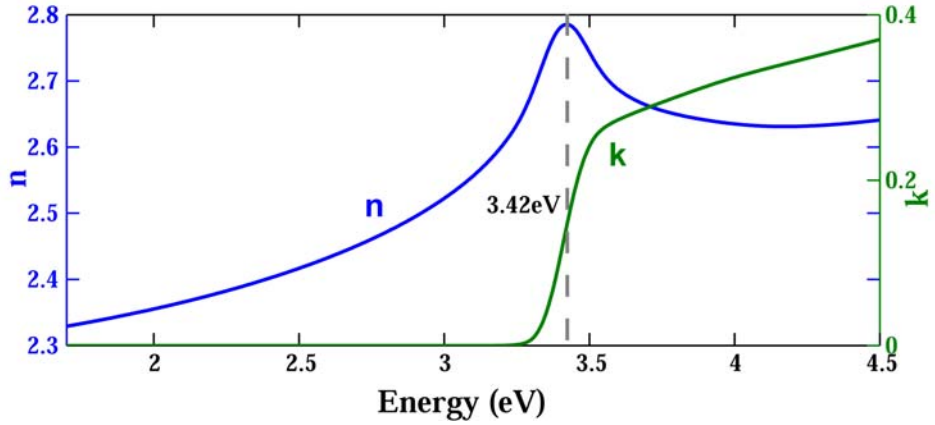

Fig. 27: Optical constants n and k calculated using AnalysR for a 5800Å GaN film on sapphire at room temperature.

However, determination of the AlGaN film band gap from the broadband reflectance is much more challenging. The larger band gap of AlGaN compared to GaN allows light with energy below the GaN band gap and above the AlGaN band gap to penetrate through the AlGaN layer but then get absorbed in the GaN layers beneath. A fraction of this light will be reflected from the AlGaN-GaN interface, which is collected by the broadband reflectance system. However, this signal, which is used to determine the band gap of AlGaN is much weaker compared to the signal arising from the GaN band gap due to the similar densities of GaN and AlGaN.

In Figure 28, the broadband reflectance spectra for 0.5 μm AlGaN on 0.6 μm GaN is shown for a large range of AlN compositions. These spectra are all calculated using AnalysR and assume a temperature of 1135°C. While there are changes between the spectra, they are not large for steps in composition of 5%.

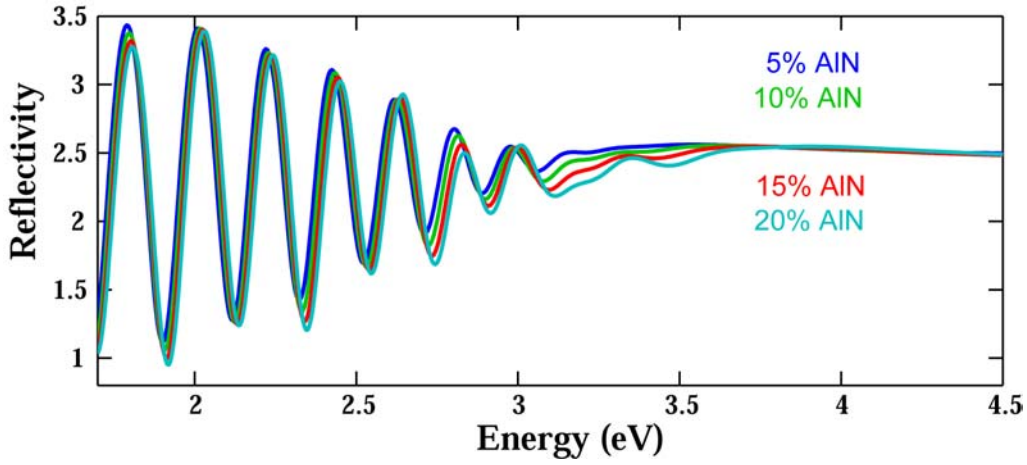

Fig. 28: Broadband reflectance spectra of 5-20% AlGaN calculated using AnalysR for T=1135°C.

In order to illustrate the strong band gap dependence on temperature the calculated band gap of AlGaN using equation (1) and (2) is plotted for different AlN% in Fig. 29.

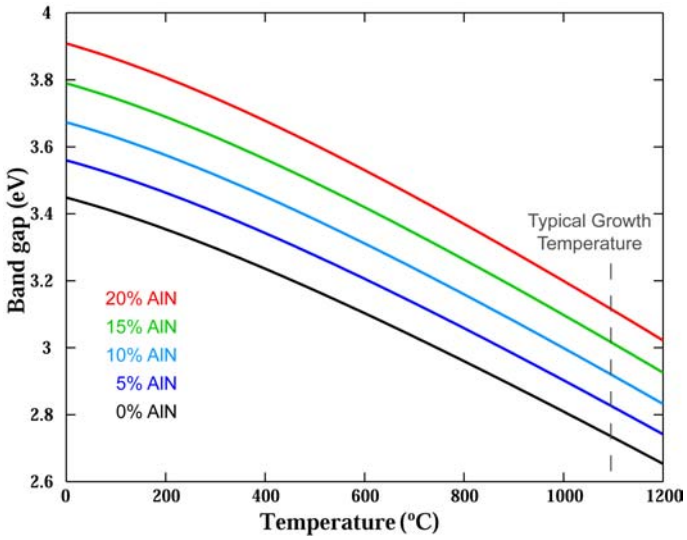

Fig. 29: Calculations of the band gap energy as a function of temperature for AlGaN films with AlN compositions of 0-20%.

The difference in calculated band gap for a 19% and 20% AlGaN is only 20 meV at 1100ºC, which is a typical AlGaN growth temperature. In addition the band gap for a given composition is reduced by 0.89 meV/K at this growth temperature. Therefore even if the band gap could be determined exactly, an uncertainty in temperature of 22ºC at 1100ºC would be equivalent to an uncertainty of 1% AlN in the AlGaN film.

Film Stress

Strain state of an epitaxial film can be related to the wafer curvature during growth, which can be monitored optically by measuring the degree of divergence of an array of laser beams reflected off the wafer growth surface. This technique, which was previously developed at Sandia, is known as multi-beam optical stress sensor (or MOSS). Such a tool was installed in a Lumileds R&D reactor and evaluated for

determining the strain state of III-nitride films during growth. Configuration of the tool and explanation of the measurement is given in Fig. 30.

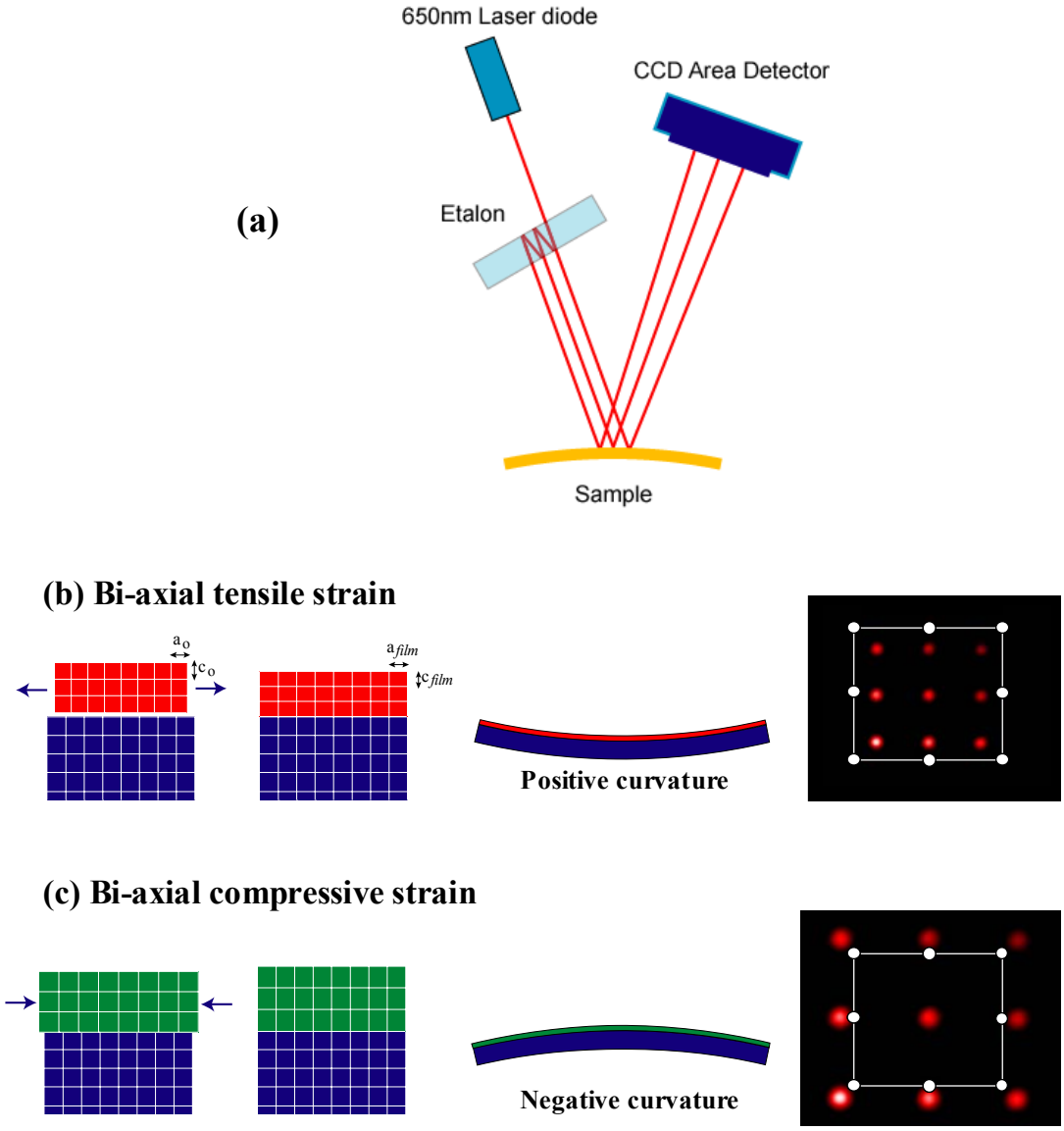

Figure 30. (a) Schematic of the MOSS tool. The effect on wafer curvature and resulting laser array pattern from biaxial strain is illustrated for (b) tensile, and (c) compressive cases.

To evaluate MOSS for determining strain state in situ, we studied layer structures including increasing levels of In (large atom, leading to compressive in-plane strain) and Al (small atom, leading to tensile in-plane strain) in either $In_xGa_{1-x}N$ or $Al_xGa_{1-x}N$ films grown on a GaN base layer on a sapphire substrate. The MOSS tool is able to monitor wafer curvature of the GaN base layer, and then capture the differential curvature (change in strain state) by the addition of the InGaN or AlGaN layer. The rate of wafer curvature can then be correlated to InN or AlN composition in the final film, as measured by XRD. The example for AlGaN/GaN is shown in Fig. 31. Wafer curvature can be correlated to absolute film stress

through calculations. A correlation between film stress, as determined in this manner from the in situ MOSS data, to final film composition for both InGaN and AlGaN layers on GaN is shown in Fig. 32. Similar results were obtained for Si doped GaN, and a measurable increase in the tensile stress can be correlated to the Si doping level. We note that the MOSS tool is also able to detect catastrophic events such as epi cracking during MOCVD, as was demonstrated during the growth of high AlN mole fraction films of too large thickness (beyond the critical thickness).

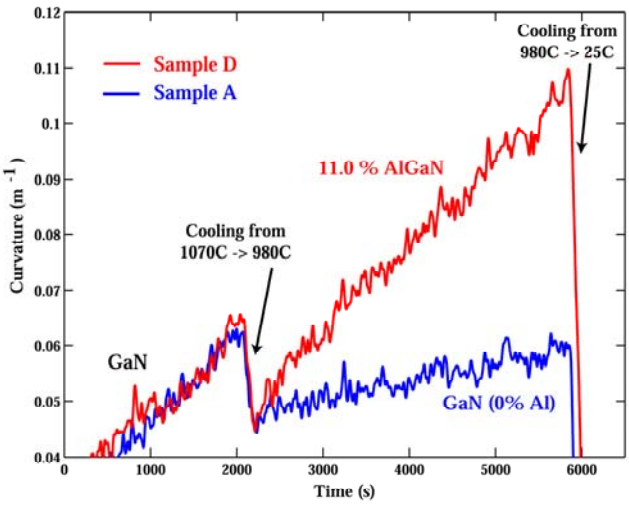

Figure 31. Wafer curvature as measured in situ by MOSS for transition from GaN to AlGaN, showing increased tensile strain in the lattice by the incorporation of Al.

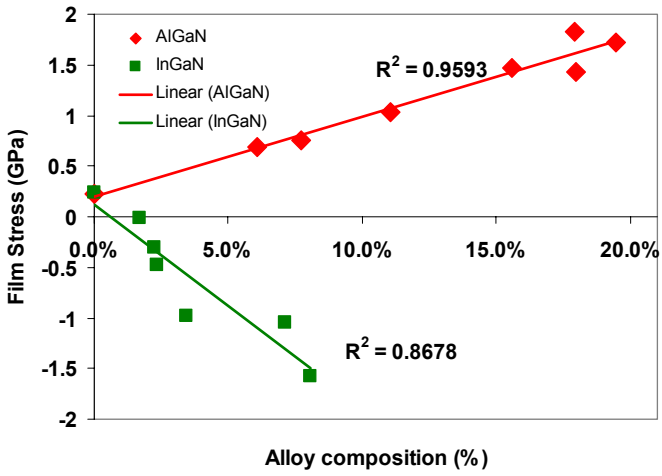

Figure 32. Correlation of film stress, as measured by MOSS, to final alloy composition for AlGaN and InGaN films grown on GaN. The strong correlation suggests MOSS could be used to measure relative changes in alloy composition, if other parameters are fixed or independently measured.

Using MOSS for composition measurement

Aluminum has a smaller ionic radius than gallium and the Al-N bond is stronger than the Ga-N bond, which results in a smaller in-plane lattice parameter for AlN (a_{AlN}=3.111Å) compared to GaN (a_{GaN} =3.186Å). When AlGaN is grown onto a GaN template and it remains fully strained to this underlying

layer, the film grows under tensile strain, as shown above, where we determined the film stress as a function AlN%. We found that increasing from 0 to 15% AlN increases the tensile film stress by 1 GPa. The effect of film stress on the band gap of AlGaN has been experimentally determined using optical absorption studies as function of applied hydrostatic pressure [3]. The pressure coefficient for AlGaN was derived to 40 meV/GPa for AlN compositions ranging from 12-60%. Hydrostatic pressure applies compressive stress to the film, and thus the band gap shrinks by 40meV/GPa with increasing tensile stress. If film stress is not measured and included in the AlGaN composition based on measurements of the band gap, a film with 15% AlN film would be off by 40meV causing an error in the AlGaN composition of 2% AlN.

Using the multi-beam optical stress sensor (MOSS), we measured the film curvature in-situ during growth of the AlGaN samples, and derived the film stress at growth temperature. Details on these measurements are described in milestone 2.08. The results are summarized in Table VI and also shown in Fig 33. The solid line in Fig. 33 represents the linear correlation between the AlN% measured by x-ray diffraction and the film stress measured using the MOSS system. The data from these AlGaN samples grown at both low and high temperature show a similar relationship. In Table VI, the AlN composition derived from this linear relationship is shown in column 6, and the difference between that and the actual AlN% measured post growth is shown in the last column. The largest deviation is 2.6% and the standard deviation for all samples is 1.26% AlN. Thus, by only using the MOSS tool the AlGaN composition can be determined. The accuracy of the measurements depends on the film thickness growth. For 3000 Å films the accuracy is 2.2%, whereas for 5800 Å films the accuracy has been improved to 0.42 %

Table VI: Summary of in-situ film stress measurements using the MOSS tool.

Sample	Temp (degC)	Thickness (A)	Slope (m-1/um)	Film Stress GPa	AlN (XRD) (%)	AlN (MOSS) %	AlN error %
A	1140	4650	0.022	0.19	0	0.55	0.55
B	1137	4090	0.059	0.53	8.28	5.64	-2.64
C	1133	3980	0.101	0.91	11.74	11.46	-0.28
D	1135	2950	0.130	1.16	17.29	15.34	-1.95
E	1138	3050	0.140	1.25	19.37	16.84	-2.53
F	973	5840	0.053	0.47	4.52	4.84	0.32
G	983	5760	0.070	0.62	6.67	7.12	0.45
H	980	5820	0.092	0.82	10.68	10.19	-0.49
J	976	3750	0.108	0.97	13.33	12.39	-0.94
						Std. Dev.:	**1.26**

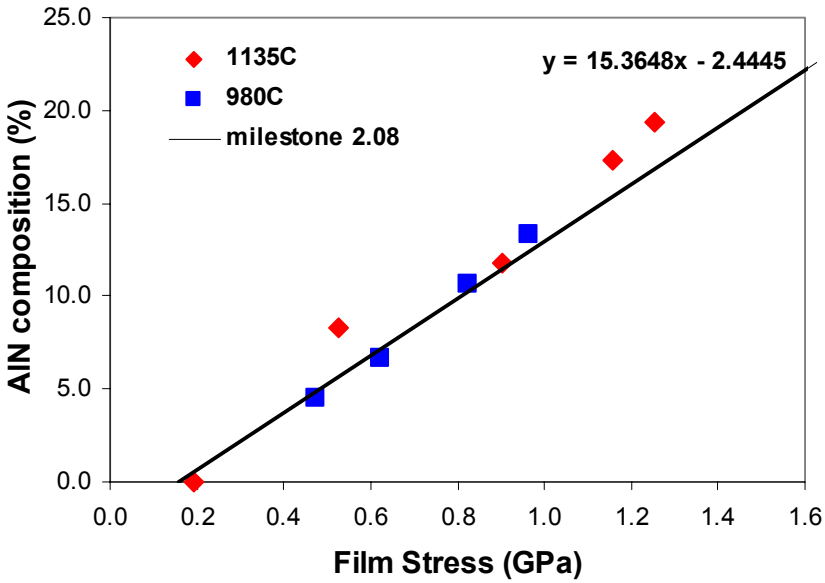

Fig. 33: AlN composition measured by x-ray diffraction plotted for all samples as a function of film stress measured in-situ using the MOSS tool. The black solid line is the correlation obtained in milestone 2.08 between the AlN% and the film stress.

Summary

We have attempted to use both *in-situ* broadband reflectance, emissivity correcting pyrometer, and stress measurements to determine the AlGaN composition based on band gap measurements. By simulating the broadband reflectance data it is clear that changes in AlGaN composition only result in small changes of the broadband reflectance, and therefore the band gap cannot be determined with much precision. In addition, the band gap only shifts slightly with AlN%. These two effects combined yield an expected uncertainty of ~5% AlN in determining the AlGaN composition during growth based on band gap measurements.

Instead of using the band gap to determine the AlGaN composition, we propose to use the stress measurements exclusively to determine the composition *in-situ.* The large tensile strain induced by AlGaN growth on GaN is shown to be a reliable method for determining the AlN%. The accuracy of the measurements depends on the film thickness growth. For example, for 3000 Å films the accuracy is 2.2%, whereas for 5800 Å the accuracy has been improved to 0.4 %.

[1] H. Jiang *et al*., J. Appl. Phys. 89, 1046 (2001)
[2] I. Vurgaftman and J.R. Meyer, J. Appl. Phys. 94, 3675 (2003)
[3] W. Shan *et al*, J. Appl. Phys., 85,8505

II-D. AlGaN Growth Chemistry

One of the disadvantages of metal organic chemical vapor deposition (MOCVD) of AlGaN alloys is the complication of accompanying parasitic gas-phase chemical reactions. An important consequence of the parasitic reactions is that the growth rate and/or incorporation efficiency become very temperature dependent at conditions where they otherwise would be nearly temperature independent (i.e. during mass transport limited growth). The growth rate (or incorporation efficiency) is also no longer a linear function of the input group-III concentration. The temperature dependence and the nonlinear concentration dependence make it much more difficult to control alloy composition. It is generally believed that reactions between ammonia and trimethylgallium (TMGa), or trimethylaluminum(TMAl), or trimethylindium (TMIn), are responsible for effectively removing group-III material from the deposition process. However, the mechanistic details of the reaction chemistry are still poorly understood. We have recently demonstrated that gas-phase nanoparticles are formed duringAlN , GaN, and AlGaN OMPVE [6,7]. These nanoparticles represent the end product of a chain of gas-phase chemical reactions. Thermophoresis keeps the nanoparticles from reaching the surface, so the mass tied up in them represents a deleterious loss of material from the gas stream.

Sandia has developed a predictive model for the AlN mole fraction incorporation for the growth of AlGaN by MOCVD taking into account the parasitic reaction mechanisms between the Al and Ga precursors and ammonia as discussed in previous reports (year 1 report, page 21 and Q3Y2 page 37). Sandia has completed a series of 11 growth runs to measure AlGaN alloy composition and growth rates over a wide range of conditions in a research rotating disk reactor (RDR). Each run typically included 3 or 4 AlGaN layers with differing Al compositions. AlGaN composition was determined with X-ray diffraction, and %Al ranged from 8-33%. For the largest experimental matrix, the surface temperature was varied from 933-1103°C at TMAl bubbler flow rates of 15, 30, 50 and 100 sccm (see Fig. 34). In all cases the solid Al composition was substantially lower than the gas-phase Al group-III mole fraction, which is one manifestation of the parasitic chemical reactions that plague AlGaN MOCVD.

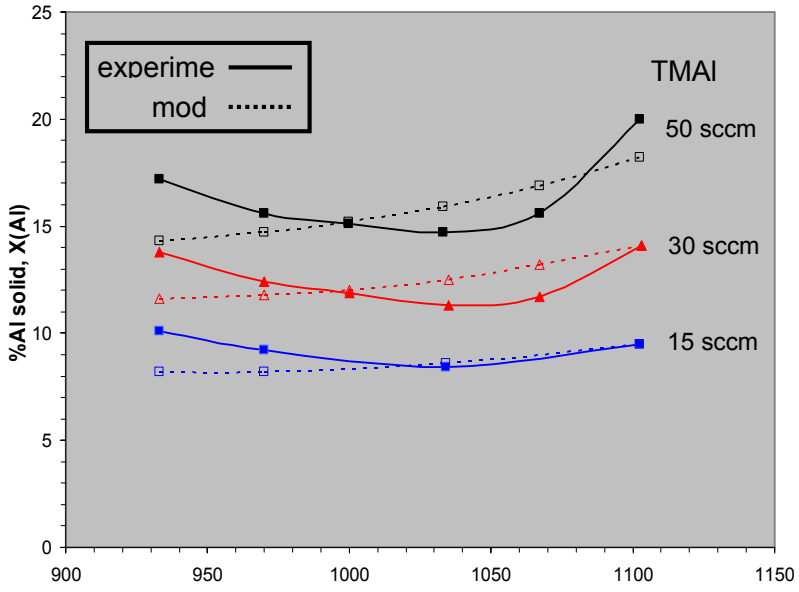

Figure 34. Al composition in AlGaN as function of temperature and TMAl flow rate at 70 torr.

The original plan was to also measure the AlGaN composition as a function of total reactor pressure, but with concerns over non-ideal RDR behavior at higher pressures we instead decided to measure the spin rate dependence. Varying the spin rate is an extremely good test for a chemical reaction mechanism because it

changes the boundary layer residence time ($\tau \propto 1/\Omega$). Increasing the spin rate tends to quench the parasitic chemical reactions and typically increases the solid Al composition.

We have synthesized a relatively simple AlGaN mechanism using the CHEMKIN/NIKE approach we developed in Q3/Y2. Currently this model includes 7 species and 10 reactions. About half of the mechanism involves particle nucleation chemistry, and half involves particle growth. The Al composition is over predicted by only 2.5-3% as a function of spin rate and the functional dependence on Ω is nearly exact. This current model is within ± 2% Al for the majority of data, but temperature trend (curvature) still needs improvement (see figure 34).

II-E. Fourier-Transform Infra-Red (FTIR) Spectroscopy for magnesium pre-reactions with ammonia during GaN:Mg MOCVD

Magnesium serves as the dominant p-type dopant for GaN and its alloys, and is typically delivered during MOCVD film growth via the organometallic precursor magnesocene ($MgCp_2$). Unfortunately, to date controlled incorporation of Mg into III-nitride films via MOCVD has not been without problems. The result often is unpredictable Mg concentration profiles that may greatly vary after the reactor has been perturbed (e.g. from changing substrates) or even from run-to-run, as has been observed in our research RDR GaN systems. Even in reactors in which the Mg doping process is largely reproducible, the Mg profile in the grown films is marked by long transients corresponding to the turn-on and turn off of the doping process. This issue, sometimes referred to as a Mg "memory effect," is problematic since sharp doping profiles are required for optimal device performance

The interaction between $MgCp_2$ and NH_3 at typical III-nitride reactor inlet conditions was examined in order to improve our understanding of Mg incorporation issues. This work represents the first in-depth investigation of the reaction between $MgCp_2$ and NH_3, and was performed using a joint experimental and theoretical approach. Our results demonstrate that complexation reactions between $MgCp_2$ and NH_3 are very likely responsible for the Mg doping "memory effects" and erratic incorporation problems.

We have spectroscopically isolated and identified two similar but distinct condensable products at room temperature—one formed at low pressures and one formed at high pressures. The IR spectra of the condensed adducts at 20 torr and 500 torr (all flow rates held constant) were presented previously (Q2Y2 page33). Both spectra show features indicative of $MgCp_2$ and NH_3 components, consistent with their assignment as adducts of $MgCp_2$ and NH_3. Because NH_3 is present in great excess over $MgCp_2$, increasing the pressure will increase the NH_3 concentration and shift the equilibrium towards the 2:1 adduct. We therefore assign the low pressure product as the 1:1 adduct (NH_3:$MgCp_2$) and the high pressure product as the 2:1 adduct ($2NH_3$:$MgCp_2$).

Based on FTIR spectroscopy experiments and DFT quantum chemistry calculations, we have isolated and identified the room-temperature products of magnesocene and ammonia as Lewis acid-base complexes. These complexes can exist as either NH_3:$MgCp_2$ or $2NH_3$:$MgCp_2$, with both adducts being condensable at room temperature. We believe the formation of these complexes can explain to a large degree the Mg doping issues observed during MOCVD growth of p-type GaN and other III-nitrides. An improved quantitative understanding of adduct condensation should allow for reactor design modifications and determination of film growth conditions that reduce or eliminate the Mg incorporation problem

II-F. Emissivity Correcting Pyrometry (ECP) for Improved Color Control

Background

Excessive run-to-run color variation in consecutive InGaN/GaN MOCVD growth runs is a major barrier to obtaining high yields in LED manufacturing. This causes a higher yield loss against the color target (non-useful inventory) and an effective artificial reduction in factory capacity. The net result is a major impediment to reducing LED cost and thus to accelerating market acceptance of solid-state lighting. Although a general correlation between growth temperature and InGaN/GaN LED wavelength is well known, the primary issue is the inability to accurately measure temperature of the growing epi layers. This is especially a problem in longer-wavelength LEDs because of the degree of control required (< 1ºC at temperatures of 700-800ºC).

For conventional III-V materials systems like GaAs, commercial pyrometer systems operating in the visible and NIR spectral regions are available to measure temperature of the substrate or epi layers directly. However, both sapphire and GaN are transparent at these wavelengths, ruling out this straightforward method for temperature measurement in InGaN/GaN LEDs. Instead, III-nitride reactors typically employ NIR pyrometers viewing the back (or under) side of the wafer carrier ("back-side" pyrometry) to obtain a relative temperature reading. This method exhibits poor correlation to final LED emission wavelength and a new approach is highly desirable. Improved results are expected if NIR pyrometers look at the topside of the reactor hardware. Also, it is possible, however, to measure the near-UV thermal emission from the growing GaN layers, using the 405 nm pyrometer developed at SNL.

Development of UV pyrometer at Sandia

Surface temperature measurement during AlGaInN MOCVD is particularly difficult because the epilayers and substrates (e.g. sapphire) are transparent at the wavelengths normally used for pyrometry (typically near-IR). We have investigated an alternative pyrometer approach to deal with the transparency problem. In this approach 400 nm pyrometry was developed because GaN epilayers are opaque at the high temperatures encountered during deposition. Various methods of emissivity-correction (EC) were applied to improve the utility and accuracy of the pyrometer.

The UV pyrometer approach uses light emission near the bandgap of GaN. The difficulty here is the small amount of thermal emission that occurs at these short wavelengths. Fortunately, the bandgap of GaN shifts from the UV into the visible (420-440 nm) as the temperature is raised to near 1000°C. The literature regarding the high temperature optical constants for GaN is rather sparse (most is extrapolated from lower temperatures), so there is some uncertainty as to the minimum wavelength required to achieve opacity. A major advantage of working in this wavelength range is the exponential response with temperature (Wien limit), which significantly reduces the sensitivity to emissivity changes.

Sandia had previously developed a pyrometer (non-EC) with an effective wavelength of 415 nm and the results showed that opacity is achieved for a GaN thickness of ~0.5 microns at typical growth temperatures (1000-1050°C). This first version used a GaP photodiode, and a very good signal to noise ratio was achieved above 1000°C. The lower useful temperature limit is in the 850-900°C range, which is due to noise and drift in the analog electronics.

Because InGaN is typically grown in the 750-800°C range, we examined methods of extending the violet pyrometer to lower temperatures. "Back-of-the-envelope" calculations showed that we should expect 10^3-10^5 photons/sec for InGaN conditions, so we decided to use a photon-counting photomultiplier tube (PMT) as the detector. Due to the shift in GaN bandgap we were also concerned that we might have to shorten the wavelength somewhat. From the filter set chosen and measured, we expected the effective wavelength to be 405 ± 2 nm. The best fit to the calibration data yields $\lambda = 405.6$ nm.

After some initial tests we also decided to add emissivity correction to this pyrometer, using the basic approach described by Breiland [1]. Some aspects of the hardware and software are different for the

PMT-based pyrometer, but the basic idea is the same. An external and chopped beam of light is reflected off the surface where the emission is also being collected. The data collection software separates the AC component (reflectance) from the DC component (thermal emission). If the sample is opaque and specular, then the emissivity (ε) = 1 – R, which is then applied to compute the corrected temperature. The success of this approach depends on a number of factors; the most obvious is the quality of the reflectance data.

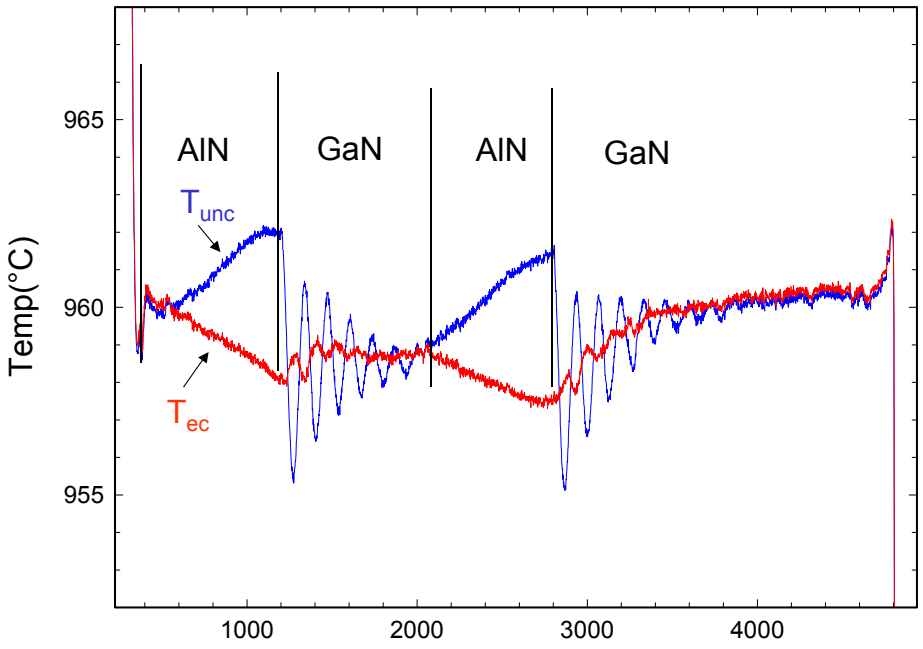

Figure 35. 405 nm ECP for GaN/AlN MOCVD at 960C.

Damped oscillations observed during the GaN growth (Figure35) demonstrate that the film is absorbing at this wavelength and temperature, as expected. During AlN deposition the non-ECP temperature rises about 2°C, while the ECP temperature falls about 2°C. During GaN deposition the non-ECP temperature exhibits damped oscillations with initial amplitude of 6-7°C. The ECP exhibits small oscillations of about 1°C of opposite phase.

The ECP results are a definite improvement over the non-ECP results, but the small residual oscillations seen in the data are almost certainly not true temperature oscillations. Previous extensive testing at Sandia (Breiland) on AlGaAs layers demonstrated that a number of artifacts can arise that lead to imperfect emissivity correction. These artifacts almost always lead to small temperature oscillations of opposite phase (compared to the non-ECP), an effect Breiland termed “over-compensation”. There are hardware methods of minimizing the artifacts, and software methods for accounting for these errors.

The other major test of the PMT-based pyrometer is temperature measurement in the 750-800°C range during InGaN deposition. Results during our second run for InGaN/GaN at 778°C, taken with a 1 Hz integration time (Figure 36), indicate that the peak-to-peak noise is ~2.5°C, corresponding to a rms noise of 0.52°C. This is pure intrinsic shot noise, so the only method of improving Signal/Noise is to integrate longer, or increase the signal level. Longer integration times are probably acceptable for some applications, but there is always an upper limit. We believe we can recover some signal (maybe X 2) through improved filters and optics, and if we decide we can work at longer wavelengths (e.g. 415 nm) we can recover another 2-3x.

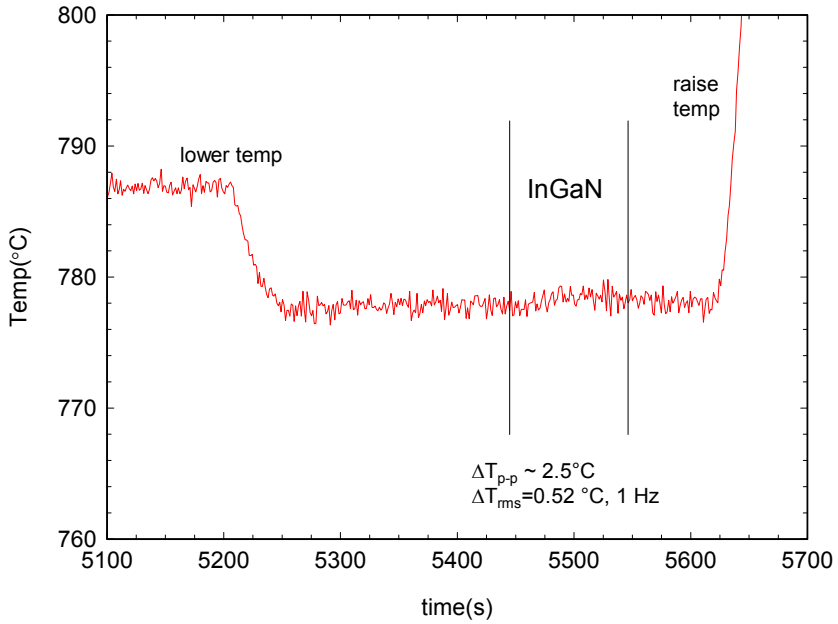

Figure 36. 405 nm ECP during InGaN growth at 778C.

In this example, the emissivity change is very small (~0.01) when the thin InGaN layer is deposited on GaN, so the ECP value is virtually identical to the non-ECP temperature (not shown). More complex structures may demonstrate the need for emissivity correction during InGaN MOCVD.

The initial tests of the 405 nm ECP with PMT detector look very promising, but more work is needed to test and refine the instrument. One problem we didn't discuss is the possible non-linearity in the PMT response at the high-count rates encountered above 1000°C. The stray light issue, which is probably the main source of error during ECP, needs further examination. It is possible the stray light problem is much worse in a radiatively heated reactor (the Sandia research reactor is inductively heated) and could limit the utility of 400 nm pyrometry.

Comparison of ECP approaches

An experimental 405 nm (UV) pyrometer, developed at Sandia National Laboratory (described above), and a single-wavelength (NIR) pyrometer were both installed on a horizontal-flow, single-wafer Lumileds R&D MOCVD reactor. The UV pyrometer was mounted on the top-view port of the reactor, looking through the port directly at the substrate, collecting the UV portion of the thermal emission at normal incidence. The NIR pyrometer, a standard commercial unit, was mounted on a side-view port of the reactor, collecting the NIR portion of the thermal emission from the topside of the wafer carrier close to the substrate ("top-side" pyrometer). A schematic of the reactor chamber cross section is shown in Figure 37. The reaction chamber is contained within a rectangular quartz liner and the substrate is situated above a SiC-coated graphite susceptor that is contained in a quartz cup. The RF coil that heats the susceptor is positioned outside the quartz liner directly beneath the quartz cup.

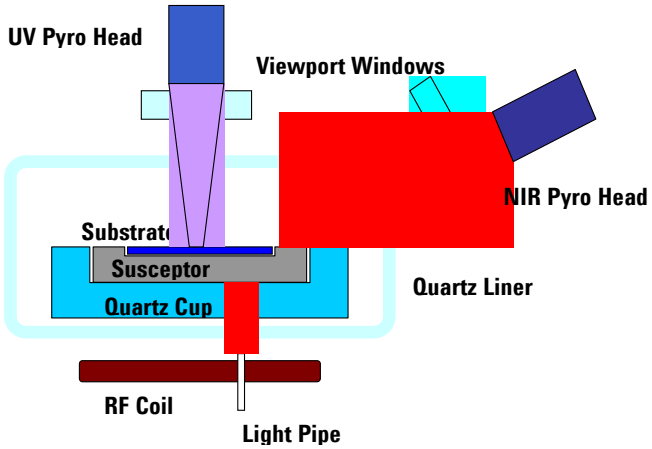

Figure 37: Schematic of a cross section through the reactor chamber. A conventional "light pipe" pyrometer positioned below near the RF coil "looks" at the backside of the susceptor. The new topside NIR pyrometer is mounted on a side-view port of the reactor collecting radiation from the graphite carrier near the substrate. The new UV pyrometer is mounted on the top-view port collecting radiation from the wafer.

In this and many other reactors, temperature measurement is typically attempted using a "light pipe" looking through the RF coil at the backside of the susceptor. The light pipe signal is converted to a temperature reading that is compared to the current temperature set point. The RF power is adjusted to match the temperature reading and set point. During regular operation of MOCVD reactors, typically chamber parts are exchanged at regular intervals due to deposits from precursor reactions. Because of fabrication tolerances, aging and slight variations in placement of these reactor components, the resulting substrate temperature often shifts when hardware is replaced despite similar temperature readings at the backside of the susceptor. This variation in substrate temperature is, in large part, responsible for the resulting large spread in emission wavelength of LEDs grown by the MOCVD process.

In this experiment, key hardware components (quartz liner, quartz cup, susceptor and wafer carrier) were randomly changed before each run to simulate the worst-case situation, where color control would be most challenging. For all of the growth runs, the target PL emission wavelength was 540 nm. A commercial Accent PL mapping system was used to generate the PL spectra, using a HeCd laser operating at 325 nm, with an output power of 5.5 mW. PL spectra were taken at the center of each wafer, and the PL peak wavelength determined by a Gaussian fit to the spectra.

In March 2003, ten wafers were grown in this reactor, using random hardware sets and the standard light-pipe temperature control, to establish a baseline against which to measure future improvement. The results are shown in Figure 38. Due to the fact that the conventional temperature measurement did not account for run-to-run hardware variations, color targeting for the baseline control runs was poor and the average wavelength from the ten runs grown was 513.9 nm. The color range (max-min) was 49.6 nm, and the average deviation from target was 26.9 nm. In a production situation, such behavior would result in poor color yield.

In the previous color-control experiments performed in April 2003, we used only the Luxtron NIR pyrometer signal to adjust the growth temperature of the active layer. Although the average wavelength of 531.9 nm was much closer to the correct wavelength target of 540 nm, there was little (~10%) improvement in the max-min range of consecutive runs. In this case, we were able to achieve a max-min color range of 44.9 nm, and an average deviation from target of 14.5 nm.

For the most recent set of color control experiments, performed in October 2003, we used a combination of both the top-side NIR pyrometer collecting thermal emission from the graphite carrier near the wafer and the 405 nm UV pyrometer collecting the UV emission from the wafer itself. The mounting scheme for the NIR pyrometer was modified to allow greatly improved, and repeatable, targeting of a

consistent location on the graphite carrier. Other hardware changes were made to accommodate the use of the UV pyrometer through the top viewport. All openings into the reactor chamber were shielded to prevent extraneous light from interfering with the weak UV thermal emission signal.

Since approximately 0.5 µm of GaN is required to achieve sufficient opacity at 405 nm to get a repeatable temperature measurement, in this set of experiments we first grew n-GaN layers on the sapphire substrates without the UV pyrometer. Because the liner clouds with deposits directly above the wafer during growth, the UV signal decreases rapidly once GaN growth commences, and the measurement becomes unreliable.

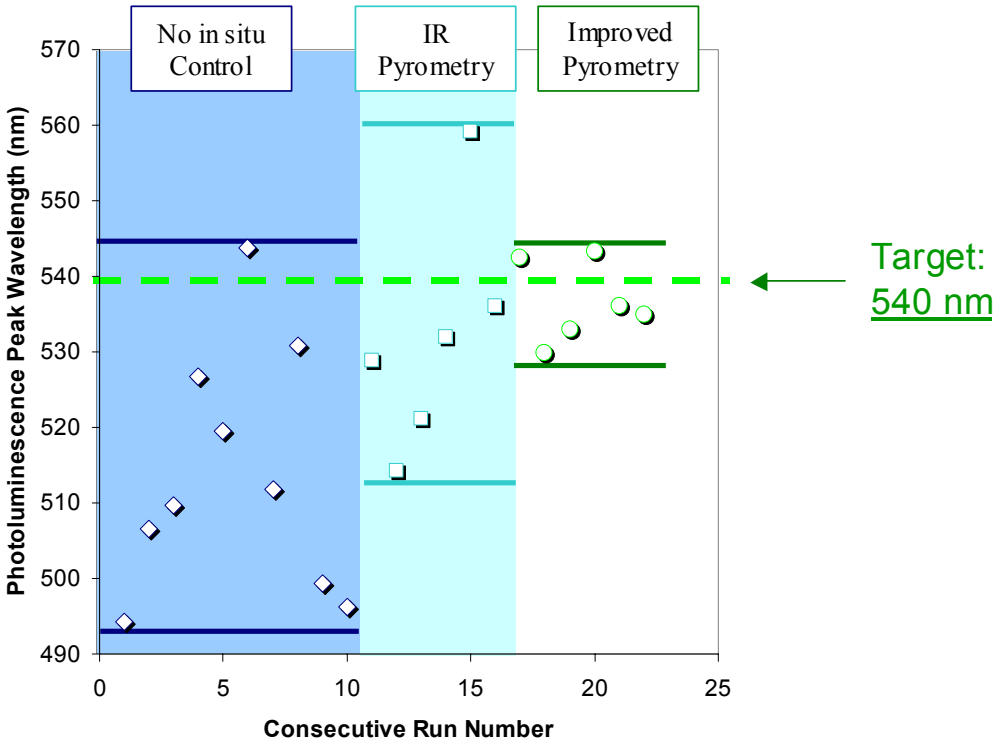

Figure 38: PL center wavelength measured for a series of LED device wafers. The data shown on the left side of the graph ("No in situ control") relate to growth runs conducted with conventional methods of temperature control. The data in the center of the graph ("IR pyrometry") relate to growth runs conducted with first-generation top-side NIR pyrometer control. The data shown on the right side of the graph ("Improved pyrometry") relate to growth runs performed using a combination of top-side UV wafer pyrometry and improved top-side NIR pyrometry of the wafer carrier.

The sapphire/n-GaN wafers were then loaded into the reactor with clean liners. During an initial heat up, the UV wafer temperature and NIR graphite temperature were both measured at several critical temperature points corresponding to "calibration" layer growth temperatures, and this data was used to generate a "correction factor" between the UV and NIR temperature measurements for that particular random hardware set combination. Then growth of the LED structure is initiated and control is performed using the NIR pyrometer only, based on the previously established UV-derived correction factor, and a method similar to that employed in the previous experiments. In this method, the active layer growth was performed in standard mode using the light pipe as temperature sensor. However, the active layer temperature set point was manually adjusted prior to active layer growth. The magnitude of the set point adjustment was derived in the following manner. The NIR pyrometer signal was recorded during growth of device layers located below the active layer in the LED structure. As a consequence these "calibration" layers are grown prior to the active layer and the NIR pyrometer readings are available prior to active layer

growth. From a large set of LED growth runs a target NIR pyrometer reading for these "calibration" layers was derived by correlating all "calibration" layer NIR pyrometer readings to resulting emission wavelength. For the growth runs shown in Figure 38 (green data points), the "calibration" layer NIR pyrometer readings were recorded and compared to the target set point. The measured deviation from this target was then applied to the active layer set point prior to the active layer growth. In this method only one temperature sensor (light pipe) is used to control RF power, avoiding potential control loop tuning problems.

Using this method, substantial improvements in both color targeting and max-min range have been demonstrated, as shown in the green data points on the right side of Figure 38. By applying a combination of both UV and NIR topside pyrometry, an average wavelength of 536.6 nm was achieved over six runs, compared to the target wavelength of 540 nm. In addition, the max-min color range was decreased to 13.5 nm, a 3.7X improvement over the 49.6 nm range of the baseline control runs, while the average deviation was decreased by a factor of over 5X to 5.3 nm, vs. the 26.9 nm deviation of the baseline runs. These results are summarized in Table VII, in comparison to the baseline runs and the previous color-control runs performed in April 2003.

Table VII: Summary of wafer center PL wavelength data for growth runs with and without pyrometer control. The NIR-only control experiments were performed in April 2003 and the results previously reported. The UV/NIR control experiments were performed in October 2003.

Criterion	Baseline	NIR Control	UV/NIR Control
No of runs	10	6	6
Target Lambda	540 nm	540 nm	540 nm
Average Lambda	513.9 nm	531.9 nm	536.6 nm
Median Lambda	510.8 nm	530.4 nm	535.5 nm
Range	49.6 nm	44.9 nm	13.5 nm
Largest Deviation	45.8 nm	25.7 nm	10.2 nm
Average Deviation	26.9 nm	14.5 nm	5.3 nm

Summary

Using a novel method, combining both a 405 nm UV pyrometer (developed by SNL) looking at the wafer surface with an infrared pyrometer looking at the top surface of the wafer carrier in an MOCVD reactor, we significantly improved color targeting and range for InGaN/GaN green LEDs. A series of six runs using the dual pyrometer control exhibited an average wavelength of 536.6 nm, compared to a target of 540 nm. The color spread was 13.5 nm. A preceding set of ten baseline or "control" runs (using conventional back-side pyrometry) yielded an average wavelength of 513.9 and a color spread of 49.6 nm. Random hardware sets were used for all runs to ensure maximum reliance on temperature control technique. The improvements in both run-to-run color range and color targeting are a direct consequence of the new method and are the most important criteria for improved color yields in manufacturing. The average deviation from target wavelength, meaning the average of the deviations of each run from target, for the control runs was 26.9 nm, while that for the dual-pyrometer runs was only 5.35 nm, a factor of five improvement (5.03X). More importantly, the run-to-run color range was reduced by almost a factor of four (3.67X), from 49.6 nm to 13.5 nm using the combined UV/NIR pyrometer control.

The UV pyrometer allowed direct temperature measurements of the epitaxial wafers, and allowed a calculation of the temperature offset between the wafer and the carrier. Also, measurements on many wafers allowed us to measure the degree of variation between hardware sets in terms of final wafer temperature. However, the signal-to-noise problem for the UV pyrometer was high in the Lumileds test, likely because of the presence of the liner (see Fig. 37). At this point, it is not clear whether topside NIR or UV pyrometry (or both together) will ultimately be most suitable for use in production, so Lumileds' plan is that each approach will be evaluated separately on a multi-wafer production reactor.

QUANTUM DOTS

III-A. Motivation

The key motivation for this work was to evaluate the potential benefits (if any) of substituting luminescence semiconductor nano-particles ("quantum dots", or QDs) for conventional luminescent materials (i.e., phosphors) in high performance LEDs. We note that photoluminescence throughout the visible spectrum has been demonstrated from QDs based on on II-VI semiconductors. Furthermore, unlike conventional phosphors, the emission spectrum depends on the QD particle size distribution in addition to the chemistry, suggesting a potentially tunable emission spectrum.

The possibility of generating white light from a mixture of QDs with the appropriate emission wavelengths is very attractive for solid state lighting. However, a great deal of scientific investigation is required for these materials to be usable in such major technology applications. In particular, the QDs must be incorporated into a suitable medium (or "binder") in order to be applied to the LED chip. In addition, the QD density must be high enough that a majority of the LED light is absorbed in a short distance, preferably 1 mm or less. In this work we studied the optical properties of nanosize CdX materials in great detail in dispersed form in nonaqueous solution. Then, the stabilization of QDs in a polymeric matrix was attempted, and the variable temperature photoluminescence experiments were performed on thin films of QDs for the first time. Finally, such films were applied directly to packaged high power LED chips, and evaluated in terms of efficiency, absorption, and other key parameters.

III-B. Synthesis & Encapsulation

CdS and CdSe quantum dots (QDs) were synthesized at SNL by Jess Wilcoxon and Steve Woessner, using metathesis reactions. Starting with simple salt precursors (e.g., $Cd(NO_3)_2$, $(NH_4)_2S$, Li_2Se) the QDs are grown at room temperature in volatile coordinating solvents like tetrahydrofuran (THF). Room temperature synthesis enables slow growth of monodisperse QDs with potentially fewer defects and 90-100% product yield. The QY is typically higher for these QDs. Room temperature synthesis is safer, more manufacturable and scaleable than high temperature methods which use pyrophoric organometallic precursors. Additionally, size selective precipitation is required to increase the monodispersity of QDs produced at high temperatures, but this process gradually removes the stabilizing organics, resulting in yield reduction.

The CdS and CdSe QDs used in this study were prepared by metathesis reactions in THF and are monodisperse with a diameter of ~2 nm (**Figure 39**). One 2 nm CdS QD has only ~85 formula units, and enormous specific surface area. Because the majority of the atoms are surface atoms, a combination of both size and surface chemistry controls the emission color. Alkylthiols (C_xSH) and tri-octylphosphine (TOP) were the stabilizing organics for CdS and CdSe, respectively.

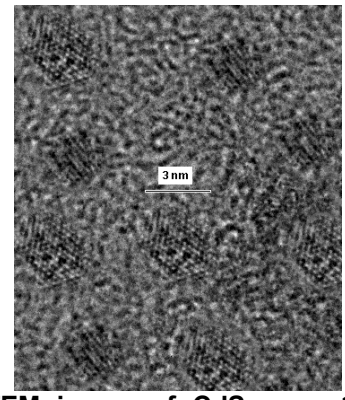

Figure 39. High-resolution TEM image of CdSe quantum dots grown in THF by J. Wilcoxon, SNL.

To make use of QDs in high power LEDs for SSL, they must be removed from a solvent environment and incorporated into polymeric encapsulants without losing their quantum size effects, surface stabilization, or quantum yield. The concentration of QDs must be sufficiently high to eliminate leakage of the LED excitation light through the encapsulant. Requirements for LED encapsulants include: transparency; high refractive index; chemical stability in the presence of UV, moisture, and elevated temperature (~100^{o}C). In this program, both epoxy and silicone were investigated.
The encapsulation part of the program involved Steve Thoma, Arturo Sanchez, and Lauren Rohwer.

Epoxy -

Our best results were obtained with blue-emitting CdS (sample #157c) in THF. The CdS QDs in THF were dispensed into a vial and evaporated in a vacuum oven at 50^{o}C until the solvent was removed. Next, a two-part epoxy (Pacific Polytech PT5-42) mixed in a 1:1 ratio, was added to the evaporated QDs, and thoroughly mixed. The QD-epoxy mixture was degassed in the vacuum oven at 50^{o}C, then poured into a machined, two-part Teflon mold with an optical flat to create disks measuring 10mm diameter x 2.5mm thick. Both CdS and CdSe QDs were incorporated into epoxy without loss of QE, indicating good dispersion.

Silicone –

The QDs were not easily incorporated into silicone. The main problems were lack of curing and loss of QE upon encapsulation. The four silicone chemistries we evaluated are described below:

- *Addition cure, Pt-catalyzed*

This system did not cure due to poisoning of the catalyst by S and Se.

- *Peroxide-activated cure*

The QD emission was lost, possibly due to degradation by peroxide radicals. Complete curing was not achieved.

- *UV cure*

Complete curing was achieved, but the acrylate groups presumably caused complete loss of QD emission.

- *Low-viscosity, amine-functionalized siloxane (S-40)*

Complete curing was achieved, but with reduction of QD emission and spectral blue shifts of orange-emitting CdS QDs.

Our best results were obtained with the S-40 silicone formulation from Vendor 1 (V1), with epoxy crosslinker. One drop of the crosslinker was mixed with 1 g of the S-40 silicone and degassed in a vacuum chamber. The QD solution was then added to the degassed silicone, thoroughly mixed, followed by another degassing step to remove the solvent. The QD-silicone mixtures were poured into a two-part mold and cured at 150^{o}C for 1 hour.

III-C. Optical Characterization

The CdS and CdSe quantum dots (QDs) were characterized at SNL by Lauren Rohwer and Billie Abrams, using photoluminescence (PL), quantum efficiency (QE), and quantum yield (QY) measurements. The QE/QY measurements were performed using a measurement system and mathematical procedure developed under SNL's Laboratory Directed Research and Development (LDRD) program. Based on absorption of diffuse light within an integrating sphere, this system requires minimal sample preparation, accounts for spectral energy distribution of the emitted light, detector responsivity, Xe lamp fluctuations, scattered and stray light, and enables accurate measurements when as little as 1% of the incident light is absorbed. With this technique we are able to reproduce the established QY for the fluorescence standard quinine sulfate dihydrate to good accuracy and precision. Samples with absorption cross-sections as small as 6 mm^2 can be accurately measured. A diagram of the system is shown in **Figure 40**. A 75 W Xe lamp

(Oriel 6251) and 1/8 m monochromator (Oriel 77250) is used to excite the samples throughout the near-UV region (360-400 nm). The grating is 1200 line/mm, and the monochromator bandpass is 2 nm. The excitation light from the monochromator is focused by a 50 mm focal length lens. The focused beam enters a diffuser that is mounted on the entrance port of a 4 in. diameter integrating sphere (Labsphere, IS040-SF/IG). The sphere has four ports, all located around its equator: (1) excitation beam entrance port; (2) excitation light detection port; (3) emitted light detection port; and (4) sample entrance port. The diffuser is a 1.55mm thick, 6.5mm diameter Teflon disk mounted onto the end of a quartz NMR tube, and inserted into the excitation beam entrance port. A NIST-traceable silicon photodetector (Newport 818-UV) is mounted on each of the two integrating sphere detection ports, located perpendicular to the beam and sample entrance ports. The optical power meter corrects for the detector response using a multiplier. With the appropriate bandpass filters in place, the optical power of the excitation and emission light can be measured simultaneously by the two photodetectors and recorded by two optical power meters (Newport 1830C). The photodetector used to measure the incident excitation light and the absorbed light was labeled Detector A. The photodetector used to measure the emitted light was labeled Detector B. Detector A uses a filter (Newport UG-11) that transmits near-UV light of wavelengths less than 400 nm. Detector B uses a filter (Newport GG400) that transmits visible light of wavelengths greater than 410 nm.

All samples, both solids and liquids, characterized in this system were placed in quartz or Pyrex NMR tubes, and inserted into the sphere through the sample entrance port. The tubes were inserted into the sphere at an angle slightly below horizontal. The end of the tube protruded approximately one inch into the sphere, and the angle and insertion depth were kept constant. The portion of the tube outside or near the sphere sample entrance port cannot have any residual sample coating the walls. The sample residue absorbs the incident excitation light, but its emitted light would tend to exit the port, reducing the measured QE.

The photoluminescence spectral energy distribution of the samples is measured using a SPEX Fluorolog II which contains a Hamamatsu R298 S20 type single-photon counting photomultiplier tube. The raw photocurrent spectra are corrected to account for the spectral responsivity of the PMT.

The CdS QDs synthesized in this program achieved record quantum efficiencies. A joint SNL-LL paper on the performance of these high QE CdS dots is in progress. The QE was measured for CdS and CdSe quantum dots in THF or octane, and in epoxy. These values are listed in **Table VIII.** Under 390 nm excitation, the QE was measured to be 74% for blue-emitting CdS (#157c) and 71% for blue-green-emitting CdSe (#85P) in THF. The results for our best CdS and CdSe QD samples synthesized in this program are summarized in the table.

The QE of blue-emitting CdS quantum dots in epoxy was measured to be 71%. The high QE in the epoxy indicates good dispersion and stability of the QDs. In addition, there was no shift in the emission spectrum due to encapsulation, as shown in **Figure 41**.

Besides stabilizing the QDs in epoxy, the absorption of the excitation light must be maximized by increasing the QD concentration. The near-UV absorption was studied by measuring the absorbance of QD-epoxy disks. The absorbance at 390 nm of QD-epoxy disks with varying concentrations of QDs was measured. **Table IX** lists the absorbance of disks made with 0.04, 0.17, and 0.5 wt.% QDs. The fraction of incident light absorbed in a sample is given by

$$\frac{I_{abs}}{I_o} = (1 - 10^{-A})$$

where I_{abs} is the absorbed light intensity, I_o is the incident light intensity, and A is the absorbance at a particular wavelength. We were able to increase the concentration of QDs so that 90% of the incident light is absorbed in a 2.4 mm path length.

We did not achieve similar successes with silicone encapsulation. There were slight changes in the PL properties of blue-emitting CdS when encapsulated in silicone, as shown in Figure 42 for

CdS(#83A). However, the QE dropped from 51% in THF to 9% in silicone. Other CdS samples were found to have more severe spectral shifts upon encapsulation. The results of this part of the program confirm the difficulties in transferring the QDs from a stable solvent environment to polymeric matrices.

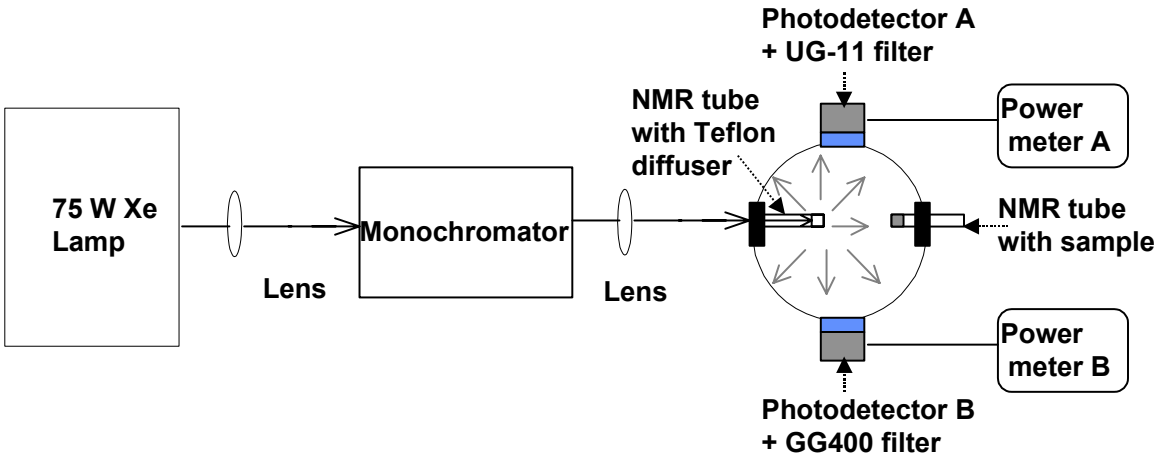

Figure 40. Schematic diagram of the diffuse light system developed for measuring quantum efficiency of liquid and solid samples.

Table VIII. Quantum efficiencies of a series of quantum dot samples tested in this system. Excitation wavelength = 390 nm.

Sample	QE (%)
CdS (#157c) in THF λ_{em} = 467 nm	74
CdS (#157c) in epoxy λ_{em} = 467 nm	71
CdS (#154d) in octane λ_{em} = 550 nm (appears white)	22
CdSe (#85P) in THF λ_{em} = 500 nm	71
CdS (#83A) in THF λ_{em} = 470 nm	68
CdS (#83A) in epoxy λ_{em} = 458 nm	43
CdS (#298) in epoxy λ_{em} = 561 nm	37
CdS (#299) in epoxy λ_{em} = 488 nm	33

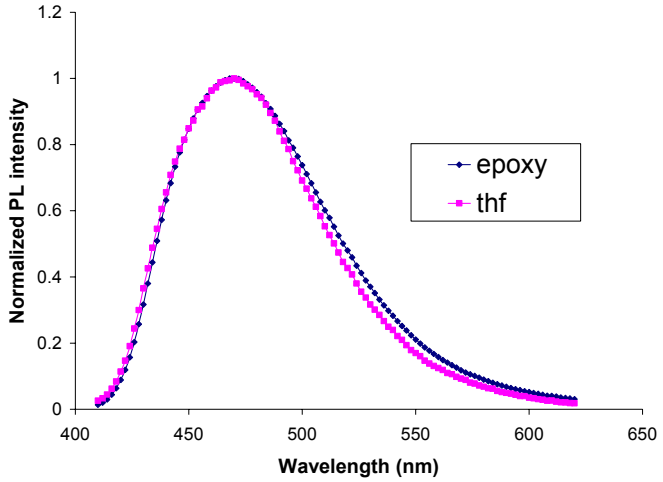

Figure 41. Photoluminescence as a function of wavelength of blue-emitting alkylthiol-stabilized CdS (#157c) QDs in THF and epoxy. The minimal shift of the encapsulated CdS emission band indicates little interaction of CdS QDs with the epoxy. Excitation wavelength=390 nm.

Table IX. Absorbance at 390 nm of CdS QD-epoxy disks (10 mm diameter x 2.5 mm thick) with varying QD loadings.

Quantum dot loading (wt.%)	Absorbance at 390 nm	$\frac{I_{abs}}{I_o}$ (%)	Path length for $I_{abs} = 0.9 I_o$ (mm)
0.04	0.17	32	13.5
0.17	0.55	72	4
0.5	0.96	90	2.4

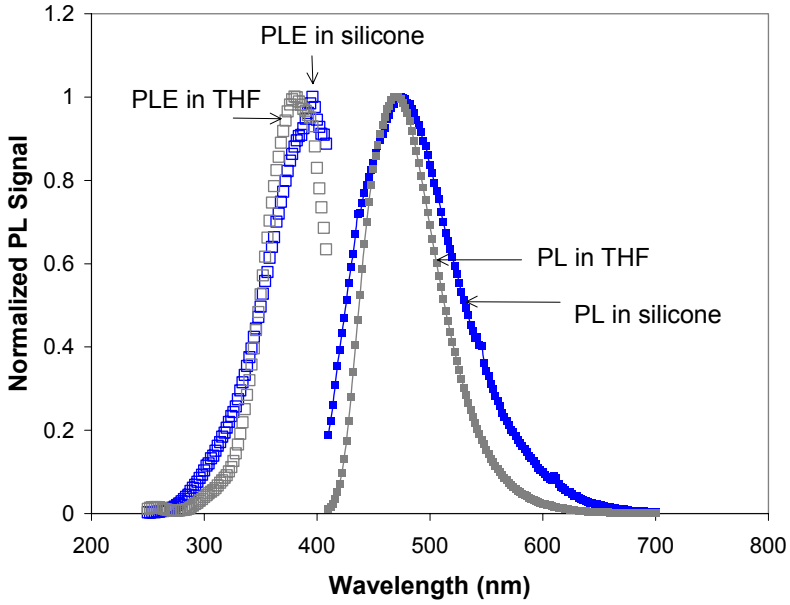

Figure 42. Photoluminescence excitation spectra (PLE) monitored at the emission peak, and emission spectra (PL) under 390 nm excitation of CdS83A in tetrahydrofuran (THF) and silicone.

Samples of quantum dots in epoxy and silicone were prepared using Teflon two-part molds to form disk shaped specimens 10 mm in diameter with a thickness of 2.3 mm. A glass cover slip was used in the mold to provide an optical flat for characterization. The quantum dot sample used (CdS157C) is a narrow-band blue-emitting material with C12SH (dodecanethiol) stabilizer on the dot surface, and dispersed in tetrahydrofuran (THF) solvent. The emission peak of this sample is 470 nm under 390 nm excitation. The Cd concentration is 2.5 x10^{-3} M.

QD-loaded Epoxy Specimen Preparation

The specimens were prepared by mixing Pacific Polytech 2-part epoxy (PT5-42H and PT5-42R) in a 1:1 ratio, adding the quantum dot solution, followed by degassing. The liquid was then poured into the mold and cured at 90^{o}C for 3 hours. The volume of quantum dot solution (CdS157C) added to the epoxy was varied from 150 µl to 2.4 ml. The absorbance of the specimens was measured using a Perkin-Elmer Lambda 19 UV/VIS/NIR spectrometer over the wavelength range 300 to 700 nm. The absorbance values at 390 nm were compared for each specimen, and are listed in Table X. Absorption lengths for 90% absorbance of the incident light were calculated based on a specimen thickness of 2.3 mm. The QD loading level in the specimens has steadily increased, and is approaching the desired level. Higher loading specimens are in progress.

Table X. Absorbance data at 390 nm for quantum dot-loaded epoxy specimens 2.3 mm thick and 10 mm in diameter.

SAMPLE	ABSORBANCE	Absorption length for $I_{abs} = 0.9I_o$ in cm
(1) 1 g epoxy + 150 µl CdS157C	0.11	2
(2) 1 g epoxy + 600 µl CdS157C	0.17	1.35
(3) 1 g epoxy + 1.2 ml CdS157C	*0.45*	*0.5*
(4) 1 g epoxy + 2.4 ml CdS157C	0.55	0.4

The quantum efficiency of sample #1 was measured to be 18%, under 390 nm excitation.

Optical Characterization at Lumileds

We obtained a series of five CdS based QD-samples. Three of them are imbedded in epoxy and emit under excitation with 400nm in blue (CdS_157b), green (CdS_299) and red (CdS_298) respectively. For the red and green emitter we obtained also the corresponding sample in THF. Different from the samples described in Q3Y2 the emission spectra for the red and green samples differ spectrally only slightly in both matrices (which might have secondary reasons, like loading point) (**Fig. 43**) and again different from report Q3Y2 the QE does not degrade too much by going into epoxy. For emission in the blue we had only the epoxy sample available, but this one shows 70 % QE at room temperature! Quantum efficiencies are summarized in Table XI for comparison with values measured at Sandia.

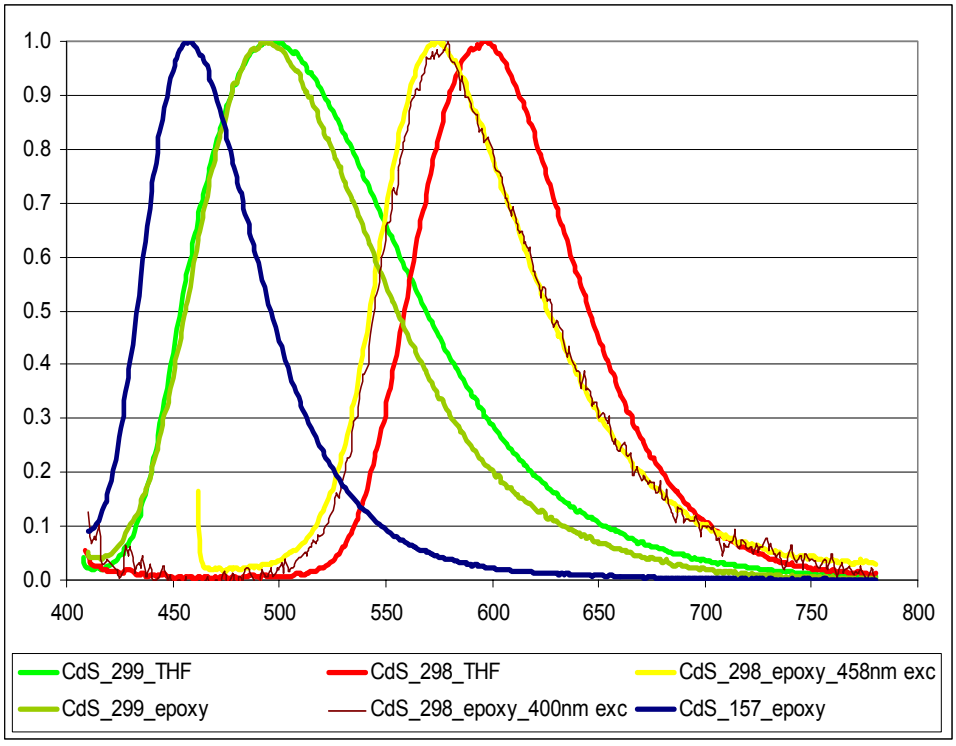

Fig. 43 Emission spectra of CdS quantum dots imbedded in THF or epoxy. If not otherwise shown in legend excited at 400 nm (laser). For CdS 298/299 a slight shift with THF/epoxy embedding is shown.

Table XI: Comparison of quantum efficiencies in THF and epoxy, measured at Lumileds.

sample	THF		EPOXY	
	QE	R	QE	R
CdS_298	31	9	4	3
CdS_299	55	3	28	6
CdS_157			70	26

We checked into the decay time of all samples at high excitation level in order to make sure that the emitters are suitable for light conversion in power LEDs. In all cases the decay time does not depend on the matrix (THF/epoxy), but differs slightly from sample to sample. CdS_157 (blue emitter) and CdS_299 (green emitter) have about 16 ns decay time, whereas CdS_298 (red emitter) has about 8 ns decay time. This is fast enough not to expect saturation problems in LED applications.

In order to get some experience with mixed white based on quantum dots some trials to mix CdS 298 + 299 (in THF) were made. This has the advantage of easier handling and should in principle teach about the expected behavior in epoxy. **Fig. 44** shows the emission spectra of the red and green component excited at 403 nm and one of the trials to get a white mixture. There is a huge difference between simple simulations (assuming no transfer from green emitter to red) and reality.

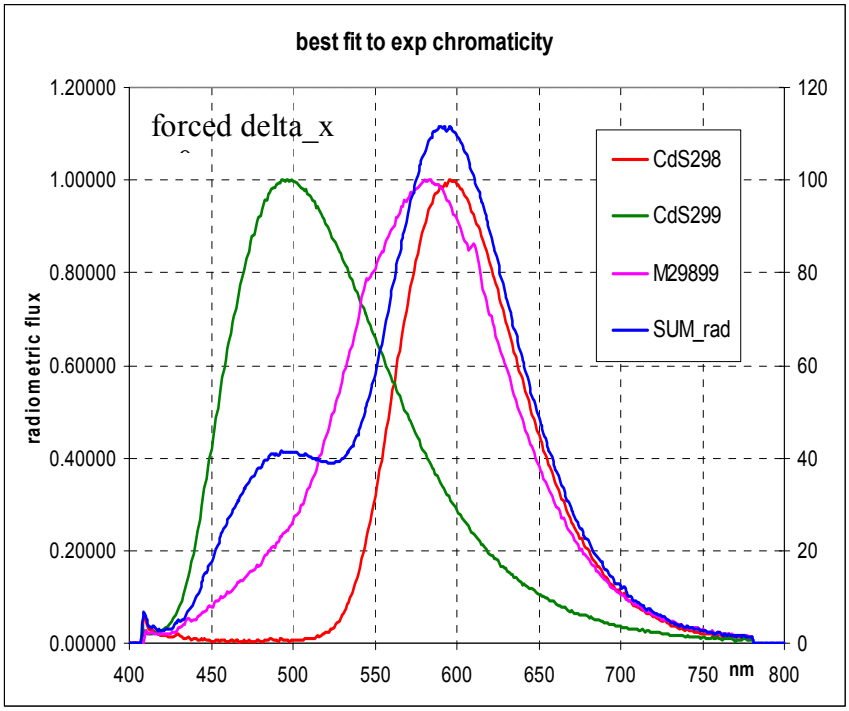

Fig. 44. Comparison of simple simulation (blue curve, SUM) and experiment (pink curve, M2298990

Fig. 45 shows the chromaticities of the two suspensions of CdS 299 and 298 in THF, as received. By mixing them all chromaticities on the straight line between them should be attainable (basic law of color science). This of course assumes that no interaction between them occurs. The experiment shows a significant deviation towards the green, Reabsorption of the emission of CdS_299 by CdS_298 is the obvious cause. By eliminating emission near 490 - 500nm the chromaticity moves towards 540 nm dominant wavelength. Fig. 45 displays the dramatic difference between a simple superposition (green) and the actual spectrum (red). Aiming at the experimental chromaticity the green superposition curve was generated as best fit. At best a color point at the line between the component color points can be generated, which is almost at the same x-value. It is useful to note that the simple superposition could achieve CCT=2880°K and a color rendering Ra=70, but not even a "white" in the sense of any standard can be achieved de facto.

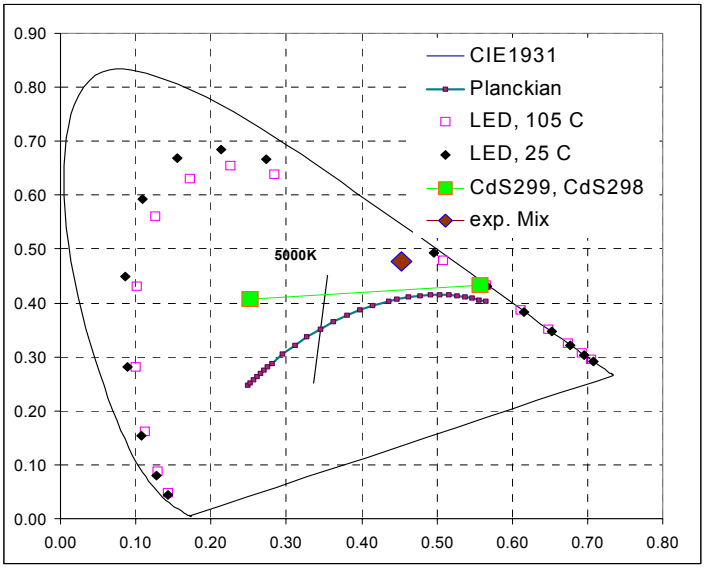

Fig. 45. The color points of two quantum dot samples (CdS 298 and 299) in solution, compared to that of their mix in an attempt to approximate

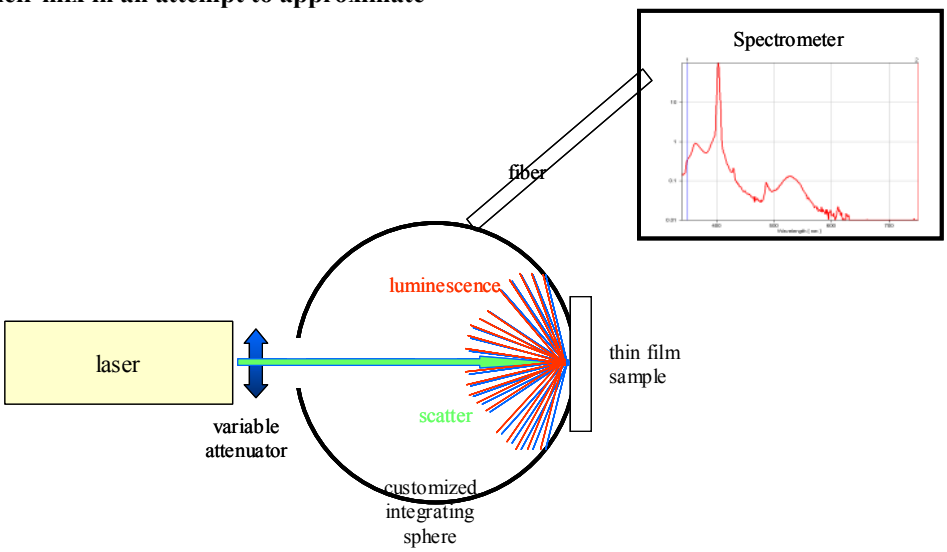

Fig. 46. Set up to measure optical scattering of quantum dot thin films.

One essential goal of the effort was and is to demonstrate that better color conversion can be achieved by using QDs instead of conventional phosphors. Two basic advantages could come to bear – absence of scattering, which lead to losses, if anywhere absorptive parts are present, and continuous choice of possible colors for optimum illumination properties. Application of QD in LEDs requires high enough absorption, high quantum efficiency (QE) to render especially the back scattering negligible relative to the luminescence generated. To draw a comprehensive picture, forward and backscattering in comparison to laser and luminescence were determined. The measurement set up is shown in Fig. 46.. As the blue and green materials were hardly excitable at 460 nm, a 403 nm laser was used. Fig.47 shows the results. All curves are on logarithmic scales, in the left parts in absolute values in the right parts normalized to the maxima.

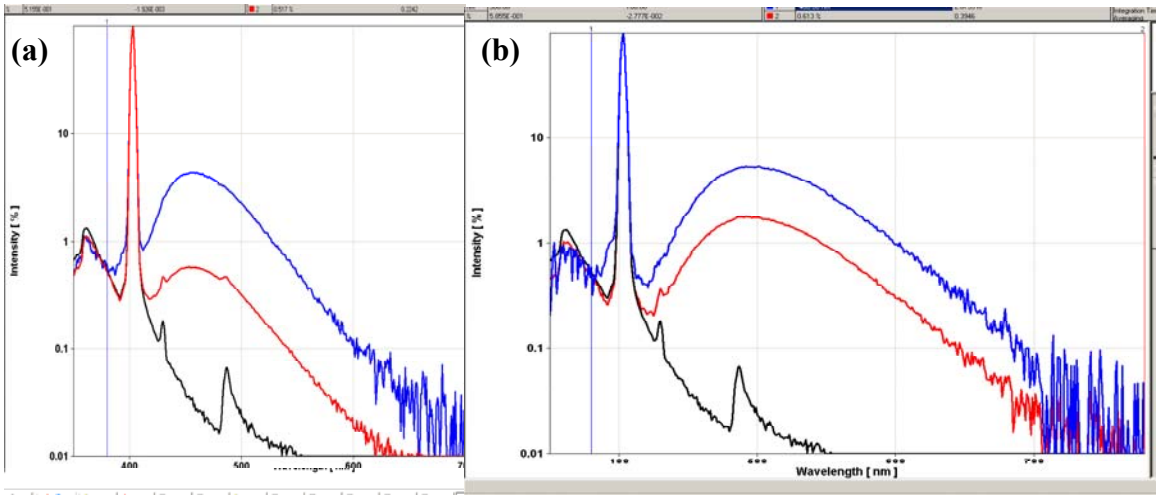

Fig. 47 Relative log scale backscatter data on (a) CdS157 and (b) CdS_299 in epoxy (black: reference, blue: back scattered, red: forward scattered).

CdS157b (blue emitting, Fig. 47a): the absorption in the 3 mm thick sample is 49%, well below expectations. Backward scattering as well as forward scattering are high – 9 and 16% of the laser power respectively. In spite of the relatively high QE (70%!), but due to the small absorption, these well convert into 116 and 152% of the respective luminescence integral.

CdS299 (green emitting, Fig. 47b): Absorption is much higher, about 80%, corresponding to an absorption length of ~ 1.9 mm (1/e). However, QE is only 30%, yielding not very different luminescence integrals. The scattering, back as well as forward, is much lower – 5 and 2% of the laser power respectively (or compared to the luminescence 70 and 20% resp.).

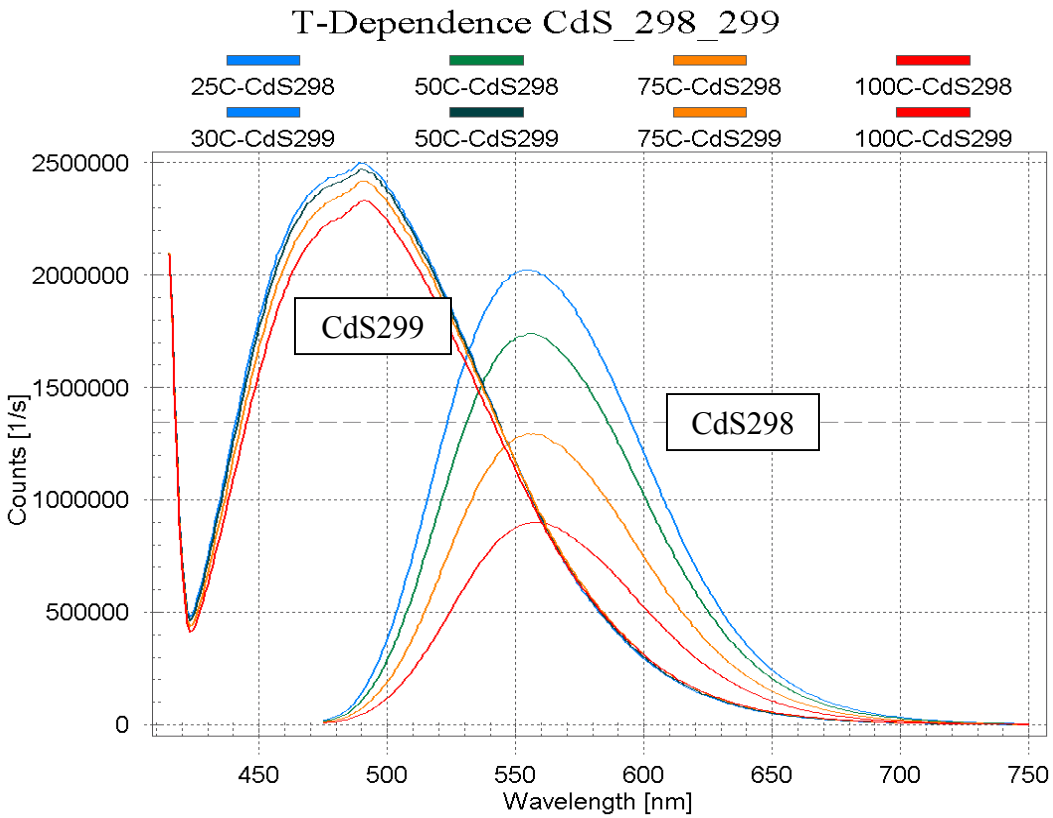

Fig. 48. Temperature dependence of CdS samples 298 and 299 from 25 to 100°C. Note intensity is measured on a logarithmic scale.

Temperature dependence

The availability of QDs in thin film form provided the capability for temperature dependent photoluminescence measurements. In Fig. 48 we compare the results for two different QD samples, CdS298 and CdS299. The temperature dependence of CdS298 (green) is rather substantial, with luminescence decreasing by more than a factor of two from 25 to 100C. However, the temperature dependence of CdS299 is observed to be rather stable, dropping by less than 10% over the same range. This performance compares reasonably well with conventional phosphors and is a good existence proof for application of QDs to LEDs, where junction temperatures can reach well beyond 100C.

III-D. LED Characterization

An attempt was made to incorporate QDs into high power LEDs. Because of the long absorption lengths, QD filled epoxy was applied over the LED, filling the reflector cup and the lens cavity, to increase the contribution of QD to the luminescence (see Fig. 49, right side). A red phosphor layer was applied directly to the chip, while the QD material was chosen to emit in the blue-green. These color points were chosen so that upon equal balance a near white appearance could be achieved. The LED wavelength was about 390 nm.

We from the electroluminescence spectra (Fig. 49, left side) that unfortunately the QD luminescence is very much smaller than the LED or phosphor luminescence, indicating again the extreme importance of high absorption in QD structures for use in LEDs.

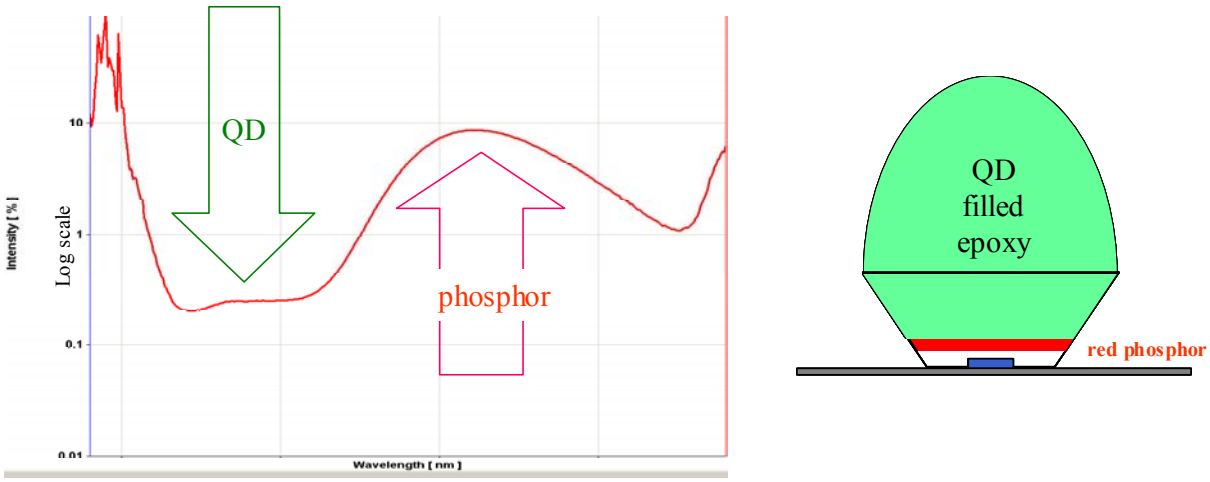

Fig. 49. Emission spectra of a high power ~ 390 nm LED employing both red phosphor conversion layer, and blue/green QD-filled epoxy. The low absorption in the relatively dilute QD-filled epoxy layer results in a very low intensity for blue-green emission as compared to red.

The availability of QDs incorporated into an LED allowed us to monitor the light output as a function of time. The results are shown in Fig. 50, for the LED with 100mA dc drive (no red phosphor layer). Surprisingly, the QD luminescence is observed to degrade rapidly within 12 min. of turn on. The cause of the degradation is unknown, and will need to be understood and eradicated before QDs can be meaningfully applied to LEDs.

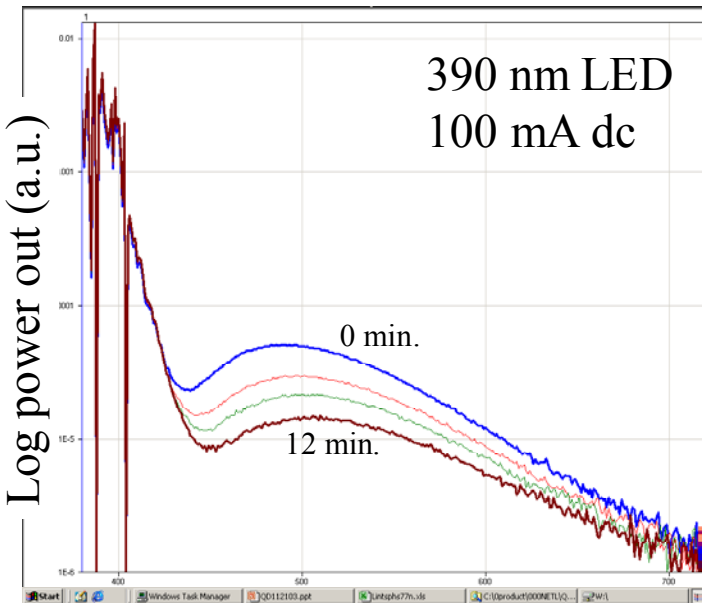

Fig. 50. Emission spectra of a high power ~ 390 nm LED employing blue-green quantum dot filled epoxy surrounding the LED chip. The blue-green portion ofht spectra is observed to decrease over time while the LED is driven (100 mA dc). The degradation is more than a factor of two over a 12 min. period.

Summary

This program fundamentally increased our knowledge about QDs and their potential application to LEDs for solid state lighting. Dramatic increases in QD quantum efficiency were achieved, with best effort samples increasing in performance from the low teens up to greater than 70%. QD thin films were shown for the first time, with quantum efficiencies as high as 70%. Also, scattering measurements on QD thin films showed the possibility for improved conversion efficiency, with measured backscatter power of only 5%, compared to conventional phosphors (~20%). However, because of the relatively low absorption in these films, the backscatter numbers must be viewed somewhat skeptically. Increased density of QDs in epoxy lead to a best-measured absorption length of 1.9 mm (1/e), far better than what is achieved in solution, although still about 10x longer than what is necessary for LEDs.

While great strides were made, we also revealed several challenges for incorporating QDs into LEDs. These include:

- Trade off between absorption length (density) and quantum efficiency
- Degradation of QD luminescence during LED excitation
- Reabsorption effects which 'collapse' broad emission spectra for mixed QDs

These challenges will need to be addressed head on, with further breakthroughs required, before QDs can be expected to play a role in LEDs for solid state lighting.

IV. RECOMMENDED FUTURE WORK

IV-A. Defect Studies

Cantilever epitaxy (CE) has demonstrated the capability to provide significantly reduced dislocation density GaN via a single MOCVD growth step. However, the direct benefit to LED performance at high currents is not observed, and is believed due at least in part to optically absorbing material deposited in the trenches during coalescence of the cantilever wings. Also, problematic leakage paths in CE-based LEDs were often observed and are believed due to partial- or non-coalescence regions proximal to the n contact layer, presumably exposed during etching in the wafer fabrication process. In order to improve the performance of CE-based LEDs and their prognosis for use in industry we recommend future work to focus on:

- Eliminating MOCVD deposition in the trenches
- Increasing the degree of coalescence possibly using thicker buffer layers
- Continuing improvement in the CE epi uniformity and percent good areas

IV-B. In Situ Tools

One of the most dramatic results from this program was the achieved improvement in green LED color control by utilizing more sophisticated ECP techniques than are currently standard for use in industry. Lumileds will continue to investigate these techniques beyond this program, in multi-wafer production reactors. AlN and InN composition measurement in situ was demonstrated using MOSS, but require relatively thick layers. For growth chemistry studies, plausible models for magnesocene-NH_3 and TMA-NH_3 reactions have been developed, and further refinement is expected to improve the predictive nature of the model and deepen the understanding of the fairly complicated (Al,In)GaN MOCVD process. We recommend future work to focus on:

- Evaluation of new ECP tools on multi-wafer production reactors
- Improve spin-rate and temperature dependence of AlGaN MOCVD model

IV-C. Quantum Dots

This program enabled the demonstration of improved efficiencies for QD phosphors, their encapsulation, and their use in LEDs for the first time. The program also allowed us to better understand the obstacles confronting the incorporation of quantum dot luminescent centers in high power LEDs. There are several opportunities for improvements in this area that must be met before QDs can compete with conventional phosphors. These include:

- Continued improvement in efficiency to enable the demonstration of QD materials with quantum efficiency greater than 90%
- Need even higher densification (abs. length <100 um) while maintaining quantum efficiency above 90%
- Need to maintain quantum efficiency greater than 85% at temperatures up to 150C
- Demonstrate reliable luminescence to 1000 hrs
- Demonstrate all the above in three primary colors (blue, green, red)

V. REFERENCES

1. C. I. H. Ashby, C. C. Mitchell, J. Han, N. A. Missert, P. P. Provencio, D. M. Follstaedt, G. M. Peake and L. Griego, Appl. Phys. Lett. **77**, 3233 (2000).
2. Carol Iris Hill Ashby, David Martin Follstaedt, Christine C. Mitchell, and Jung Han, U.S. Patent No. 6,599,362 B2, ***Cantilever Epitaxial Process,*** issued July 29, 2003.
3. A. Sakai, H. Sunakawa and A. Usui, Appl. Phys. Lett. 71, 2259 (1997); Appl. Phys. Lett. 76, 442 (2000).
4. D. M. Follstaedt, P. P. Provencio, N. A. Missert, C. C. Mitchell, D. D. Koleske, A. A. Allerman and C. I. H. Ashby, Appl. Phys. Lett. **81**, 2758 (2002).
5. D. D. Koleske, A. J. Fischer, A. A. Allerman, C. C. Mitchell, S. R. Kurtz, J. J. Figiel, K. W. Fullmer and W. G. Breiland, Appl. Phys. Lett. **81**, 1940 (2002).
6. M. P. Moran, A. K. Norman and D. M. Follstaedt, Microscopy and Microanalysis 9, Suppl. 2, 106 (2003).
7. D. M. Follstaedt, N. A. Missert, D. D. Koleske, C. C. Mitchell and K. C. Cross, Appl. Phys. Lett. **83,** 4797 (2003).
8. P.P. Provencio, D.M. Follstaedt, N.A. Missert, D.D. Koleske, C.C. Mitchell, A.A. Allerman and C.I.H. Ashby, Mat. Res. Soc. Symp. Proc. 743, L3.15 (2003).
9. C. C. Mitchell, *Defect Reduction in Gallium Nitride using Cantilever Epitaxy,* Thesis, UNM Electrical Engineering Department, 4/4/03, Albuquerque, NM.
10. L. S. Rohwer, B. L. Abrams, and J. E. Martin, "Measuring the absolute quantum efficiency of luminescent materials," *J. Lumin*., 2004 (submitted).